

**Department of Physics and Astronomy  
University of Heidelberg**

Bachelor Thesis in Physics  
submitted by

**Sophia Milanov**

born in Düsseldorf (Germany)

**2016**



# Hunting for Intermediate-Mass Black Holes in simulated Globular Clusters using Integrals of Motions

This Bachelor Thesis has been carried out by Sophia Milanov at the  
Max Planck Institute for Astronomy in Heidelberg  
under the supervision of  
Dr. Glenn van de Ven

## Abstract

In this thesis we will carry out investigations in action space of simulated globular clusters (GCs) to examine if the method of integrals of motion is useful to find signatures of intermediate mass black holes (IMBHs), whose detection is still highly controversial. We investigate four simulated GCs, two of which contain an IMBH. After analysing them in phase space, we switch to action space using the potentials derived by the density profiles. In action space we investigate the classical integrals of motion, i.e. energy and angular momentum, and particularly the radial action as best choice of integral of motion. We find signatures of the IMBHs in distributions of the radial action versus the energy, the angular momentum and the guiding-star radius. We test these signatures using a wrong potential to calculate the integral of motions and show that they are robust signatures of a presence of IMBHs.

## Zusammenfassung

In dieser Arbeit führen wir Untersuchungen simulierter Kugelsternhaufen im Wirkungs-Winkel Raum durch, um zu testen, ob diese Methode der Integrale der Bewegung nützlich ist, Charakteristika von mittelschweren schwarzen Löchern zu finden, deren Entdeckung höchst umstritten ist. Wir untersuchen vier simulierte Kugelsternhaufen, von denen zwei ein mittelschweres schwarzes Loch enthalten. Nach der Analyse im Phasenraum wechseln wir in den Wirkungs-Raum mit Hilfe der von Dichteprofilen abgeleiteten Potentiale. Im Wirkungs-Raum untersuchen wir die klassischen Integrale der Bewegung, also Energie und Drehimpuls, und insbesondere die radiale Wirkung als beste Wahl des Integrals der Bewegung. Wir finden Charakteristika des mittelschweren schwarzen Lochs in Plots der radialen Wirkungen aufgetragen über Energie, Drehimpuls und dem Leitstern Radius. Wir testen diese Signaturen mit einem falschen Potenzial, aus dem wir die Integrale der Bewegung berechnen und zeigen, dass diese Signaturen eines schwarzen Loches robust sind.

# Contents

<b>1</b>	<b>Introduction</b>	<b>1</b>
<b>2</b>	<b>Method and Theory</b>	<b>5</b>
2.1	Stellar population in globular clusters . . . . .	5
2.2	Kinematic profiles of globular clusters . . . . .	7
2.3	Density and potential . . . . .	8
2.3.1	Density of a collisionless stellar system . . . . .	8
2.3.2	Generating the potential from Poisson's equation . . . . .	8
2.3.3	Other potential models . . . . .	9
2.4	Orbits and integrals of motion . . . . .	10
2.4.1	Classical integrals of motion in spherical potentials . . . . .	10
2.4.2	The effective potential . . . . .	11
2.4.3	Actions . . . . .	13
2.4.4	Numerical orbit integration . . . . .	15
<b>3</b>	<b>Analysis</b>	<b>18</b>
3.1	Description of the globular cluster simulations . . . . .	18
3.2	Investigation in color magnitude space . . . . .	19
3.3	Investigation in phase space . . . . .	23
3.3.1	Testing for sphericity, origin and rotation . . . . .	24
3.3.2	Kinematics . . . . .	25
3.3.3	Spatial distribution . . . . .	26
3.3.4	Potential . . . . .	30
3.4	Investigations in action and integral of motion space . . . . .	31
3.4.1	Radial action versus energy . . . . .	33
3.4.2	Radial action versus angular momentum . . . . .	35
3.4.3	Investigation of stars bound to the intermediate mass black hole .	35
3.4.4	Radial action versus guiding-star radius . . . . .	35
<b>4</b>	<b>Results &amp; Discussion</b>	<b>40</b>
4.1	Signatures of intermediate mass black holes in action space . . . . .	40
4.2	Robustness of the results: using a wrong potential . . . . .	41
4.3	Discussion and future perspectives . . . . .	43
<b>5</b>	<b>Conclusion</b>	<b>45</b>

<b>6 Acronyms</b>	<b>46</b>
<b>Bibliography</b>	<b>50</b>

# 1 Introduction

Globular clusters (GCs) are self-gravitating, gas-free systems of  $10^5$  to  $10^7$  stars which are spherically grouped with a typical size of a few parsecs and mass around  $10^5$  to  $10^6 M_\odot$ . There are about 150 of them in the Milky Way (MW) (Harris, 1996). Since they are some of the oldest stellar populations in the universe (approximately 13 Gyr old), they contain much information about the assembly history and evolution of the MW. Formerly seen as very simple spherical and isotropic stellar systems with only one stellar population (Meylan and Heggie, 1997), recent research revealed a much higher degree of complexity. GCs are now known to host multiple stellar populations that challenge our understanding of their formation (that differ in the light-elements abundances, Piotto *et al.*, 2015). Moreover, GCs now also appear dynamically complex, presenting deviations from spherical symmetry, anisotropy in velocity space and significant internal rotation (see for example Zocchi *et al.*, 2012; Bianchini *et al.*, 2013; Kacharov *et al.*, 2014).

Recent attention has been devoted to the search of intermediate mass black holes (IMBHs) in the centre of GCs. These elusive black holes with masses of  $10^3 M_\odot < M_\bullet < 10^4 M_\odot$  could be the missing link between stellar mass black holes ( $M_\bullet < 100 M_\odot$ ) and super massive black holes (SMBHs,  $M_\bullet > 10^5 M_\odot$ ) (see Carroll and Ostlie 2006, p.639), as they could represent the seed for the formation of SMBHs. Their search in the centre of GCs has partially been motivated by the extrapolation of the  $M_\bullet - \sigma$ -relation for galaxies (Ferrarese and Merritt, 2000), describing the relation between the mass of a central massive black hole and the velocity dispersion of its host galaxy.

The hunt of IMBHs in Galactic GCs has been primarily based on two methods:

- 1) detection of radio and X-ray emission due to the accretion of gas in the black hole (Miller and Hamilton, 2002; Maccarone and Servillat, 2008; Kirsten and Vlemmings, 2012; Strader *et al.*, 2012);
- 2) detection of kinematic signatures in the central region of a GC (Bahcall and Wolf, 1976; Lützgendorf *et al.*, 2013).

The first method proved to be difficult because the feeding of a black hole with gas is highly inefficient in a gas poor environment like the one of Galactic GCs.

The kinematic detection of IMBHs is usually based on the analysis of the velocity-dispersion profile in the inner few arcseconds around the crowded centre of a GC in search for a rise of the velocity dispersion. This requires a combination of high angular

resolution and high spectral resolving power. For this reason, the detection of IMBHs remains still highly challenging.

Currently, there are two different kinematic methods trying to detect IMBHs: resolved kinematics of discrete stars and unresolved integrated light kinematic measurements (see, for example Bianchini *et al.*, 2015). These methods often deliver significant different results when applied to the same GC. As an example, Figure 1 shows the unres-

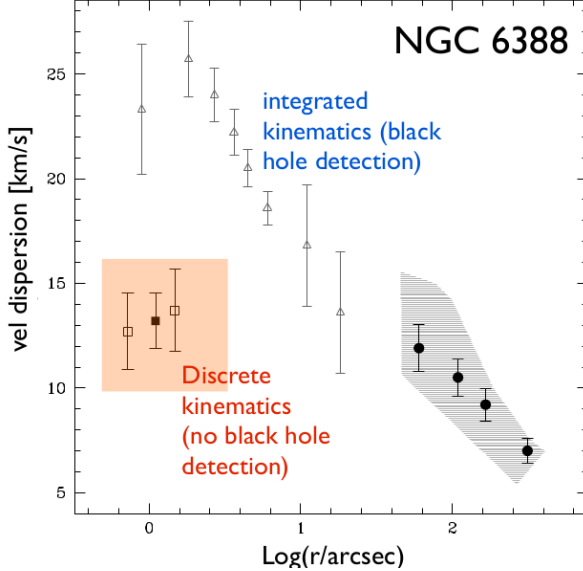


Figure 1: Velocity profile of NGC 6388 derived by the two different kinematic measurements (unresolved/integrated versus resolved/discrete). We see a cusp given by the integrated kinematics method, indicative of the presence of an IMBH, while no cusp is observed with discrete kinematics. Figure adapted from Lanzoni *et al.* (2013).

solved/integrated IFU kinematics which result in a signature of an IMBH for NGC 6388 (cusp in the velocity dispersion profile, Lützgendorf *et al.*, 2011) and resolved/discrete kinematics which do not yield IMBHs (no cusp in the velocity dispersion profile, Lanzoni *et al.*, 2013).

The first proposed detected IMBH of a GC using integrated light IFU kinematics was in  $\omega$  centauri (Noyola *et al.*, 2008) observing a rising velocity profile. Two years later, van der Marel and Anderson (2010) used Hubble Space Telescope (HST) proper motions and a different photometric centre and they could not detect the IMBH. From then, many additional investigations were done for this GC, unsettlingly giving contradictory results. For example, using the method of detection of X-ray emission there was no IMBH found (Lützgendorf *et al.*, 2015).

Given these controversial results that prevent us from drawing definite conclusions on the existence of IMBHs in Galactic GCs, we propose to introduce a new approach to analyse the effects of an IMBH to the central kinematic of a GC. Our method consists in going beyond the traditional phase space analysis (i.e., analysis of velocity dispersion profiles), by investigating the orbit distribution functions (DFs) of GC stars. Our expectation is that an IMBH could alter the orbital properties of the stars that more closely interact with it.

An orbit is the path an unperturbed, collisionless tracer particle (e.g. a star) will move along in a gravitational potential. Orbits contain information about the gravitational potential generated by the mass distribution of a system in their position and velocity coordinates following Newtons 2nd law. Orbit DFs describe which orbits are populated by how many tracers. From the orbit DF, together with the overall potential, we can draw inferences about the structure and evolution history of a stellar system.

Observations of orbits enabled discoveries or confirmed them:

- From rotation curves of galaxies we see that stars move faster than what expected by the presence of only the mass of luminous matter. There has to be more matter interacting via gravitational forces. This has led to the theory of dark matter (Rubin *et al.*, 1980).
- The orbit of Mercury differs hugely from its calculated Kepler orbit. This is because of its migrating pericentre called 'Perihelion shift'. Due to the proximity to the Sun gravitational forces are so strong that we need to apply general relativity (Carroll and Ostlie, 2006, p.609/610).
- The SMBH Sagittarius A\* with a mass of  $4.31 \pm 0.42 \times 10^6 M_\odot$  was detected by direct observations of the orbits around the black hole and resulting mass calculations (Gillessen *et al.*, 2009).

The investigation of orbit DFs proves to be a powerful tool to understand and model dynamical systems. Orbit DFs are for example widely used to describe our MW galaxy where stars of different components (thin disc, thick disc, bulge, halo) are on different orbits (dynamical distinct) and have different metallicities and chemical abundances (chemical distinct) (see for example Bovy and Rix 2013, Piffl *et al.* 2014 and Sanders and Binney 2015).

Describing orbits with the coordinates  $(\vec{x}(t), \vec{v}(t))$  is very difficult since they have a complicated time evolution in 6 coordinates. A better way to describe orbits are integrals of motion, since they are constant along the orbit. The classical integrals of motion of a spherical system are the energy  $E$  and the three components of the angular momentum vector  $\vec{L}$ . But in general the best choice of integrals of motions to describe an orbit are actions  $\vec{J} = (J_r, J_\theta, J_\phi)$  (Binney and Tremaine, 2008, p. 220/221). One of their advantages is that we can connect them with a set of angle coordinates which describe the time evolution along the orbit. Actions  $\vec{J}$  and angle coordinates  $\vec{\theta}$  form together a set of canonical conjugate coordinates. Another advantage is that they have an intuitive physical meaning: they quantify the amount of oscillation of the orbit in the different coordinate directions. That is why actions are excellent orbit labels and therefore ideal parameters for orbit DFs. Our goal is a description of orbit DFs of GCs and due to the above mentioned reasons we investigate them in action space.

In this thesis we wish to test the feasibility of the analysis of the action/orbit space in GCs and test whether it could be possible to predict signatures of IMBHs. This will be done by "translating" the traditional phase space into orbit space, exploiting the potential and the  $\vec{x}$  and  $\vec{v}$  vectors. Despite this type of information (6-D info) is not currently available for Galactic GCs, we are motivated by the growing amount of photometric and kinematic data that are already able to deliver a 5-D info (2D spatial info and 3D kinematic info); in particular the high accuracy HST proper motions (see for example Bellini *et al.*, 2014) and the upcoming GAIA data. We will limit our analysis to GC simulations with and without IMBHs to explore this approach. The thesis is structured in two parts: first we familiarize with a phase space analysis of the simulations and then we focus on how to study the orbits and extract predictions of the presence of an IMBH.

## 2 Method and Theory

In this chapter we give an overview of the theory and methods which are used throughout this thesis. We begin in Section 2.1 with the description of the stellar population of a GC. We introduce the formulas which we will use to investigate GCs in phase space by analysing the stellar kinematic profiles (such as velocity dispersion and anisotropy profiles, Section 2.2) and the spatial distribution of stars (density profiles and potential, Sections 2.3.1 and 2.3.2). In Section 2.3.3, we introduce different potential models. In the next Section 2.4.1 we define orbits and their classical integrals of motion. After explaining the benefit of the effective potential in Section 2.4.2, we show how we calculate the actions as best choice of integrals of motions (Section 2.4.3). Then we describe the numerical way of calculating orbits (Section 2.4.4) for which we also give some examples. If not stated otherwise all integrals of motions are given as specific quantities which means they are given in units of the mass of the star.

### 2.1 Stellar population in globular clusters

The typical stellar population of a GC can be visualised in a color magnitude diagram (CMD). We show in Figure 2 an example of a CMD extracted from one of our simulations (SIM 1, described in Section 3.1). In this CMD the absolute V-band magnitude is plotted against the B-V color. The color code indicates the mass of the stars. The position of a star in the CMD can be interpreted as its evolution stage. If the GC was indeed a single stellar population (SSP), i.e. all stars had the same age and metallicity, the distribution of stars in the CMD would be a function of the stellar mass only ("isochrone"), with more massive stars being in a later evolutionary stage. Most of the stars are still on the main sequence and they are characterized by hydrogen fusion in their cores. There are two main sequence lines one upon the other. These occur due to binary systems whose flux is given by the sum of the single fluxes of the single components, and therefore appear redder and more luminous. These binary systems represent about 7.5 % of the stars in this GC simulation. The turn-off point describes the moment in the evolution of the star, when hydrogen in its core is exhausted and it evolves away quickly from the main sequence towards the red giant branch. The position of the main sequence turn-off depends on the age of the system and therefore can be used as an indicator to determine the age of the cluster by comparing it to theoretical isochrones.

Bluewards of this turn-off point, following the trend of main sequence stars, there are the so called "blue straggler" stars which are remnants of stellar collisions or interacting

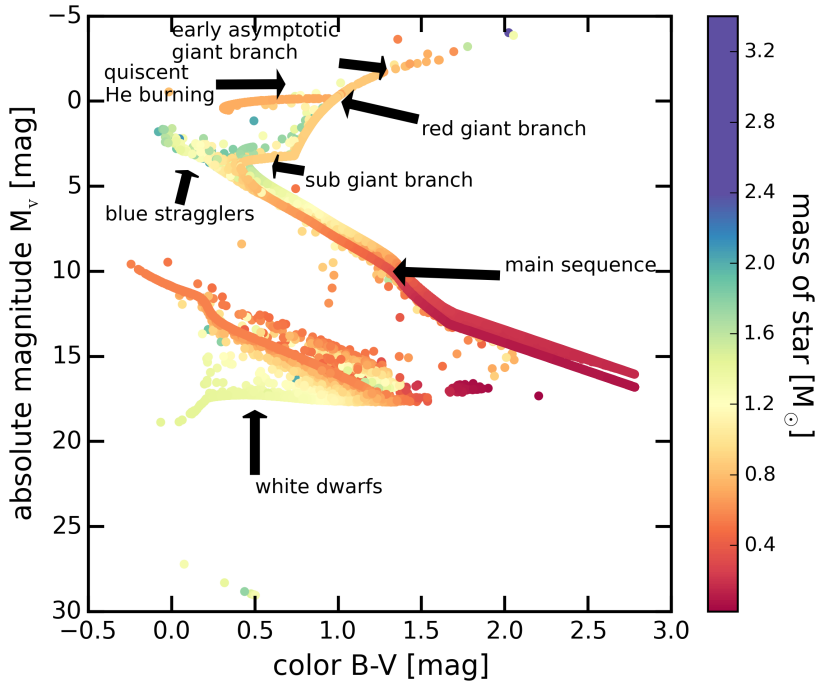


Figure 2: Color magnitude diagram of SIM 1 (see Section 3.1). The absolute V-band magnitude versus the color B-V gives us an overview of the stellar population of this GC. The stars are color coded by their masses. Since there is only one binary system having a mass of  $3.4 M_{\odot}$  and the next heavier object having a mass of  $2.4 M_{\odot}$  we set the upper limit of the color at the second highest mass. On the main sequence there are two branches. The brighter and redder sequence is caused by binary systems. Following the main sequence there is the turn-off. Bluewards of the main sequence turn-off point blue straggler stars are located. Redwards of the turn-off there is the sub giant branch followed by the red giant branch. The most luminous stars are situated on the early asymptotic giant branch. At a absolute magnitude of zero there is the horizontal branch where stars burn He quiescently. Below the main sequence and blue stragglers the white dwarfs are located. Having nearly no luminosity dark stellar remnants are situated at the bottom of the CMD.

binaries (Binney and Tremaine, 2008, p.628). Continuing from the turn off point there are the sub giant and the red giant branch consisting of stars still fusing hydrogen but only in a shell surrounding a degenerate helium core. They are inflated with a radius much higher than the main sequence stars but have a much lower surface temperature. On the upper part of the red giant branch lies the horizontal branch. Its stars burn helium in their core and hydrogen in a surrounding shell. On the early asymptotic giant branch following the horizontal branch the stars are burning hydrogen in outer shells helium in inner shells. These are the brightest stars of a GC (Carroll and Ostlie, 2006, p.476-477). In the lower left corner white dwarfs are located. They are stellar remnants which have burnt all of their resources. In a typical GC dark stellar remnants like stellar black holes and neutron stars are present but not visualised in the CMD. In this CMD we see them at the bottom of the figure.

## 2.2 Kinematic profiles of globular clusters

The stellar velocity dispersion quantifies the spread of different velocities stars can have at given positions. With the actual velocity  $v_i$  of the  $i$ -th star,  $\langle v \rangle$  specifying the mean of the velocities of all considered  $N$  stars and the second velocity moment (with the  $n$ -th velocity moment given by  $\langle v^n \rangle = \frac{1}{N} \sum_{i=1}^N v_i^n$ ) we can calculate the velocity dispersion as the standard deviation of the velocity distribution:

$$\sigma_i(r) \equiv \sqrt{\langle (v_i(r) - \langle v_i(r) \rangle)^2 \rangle} = \sqrt{\langle v_i(r)^2 \rangle - \langle v_i(r) \rangle^2} \quad i = r, \theta, \phi. \quad (1)$$

For a spherical system it is best to calculate them with respect to the spherical coordinates, i.e.  $v_r, v_\theta, v_\phi$ . If the GC contains an IMBH the velocity dispersion towards the centre is expected to increase.

The preferred direction of the motion of stars can be related to an anisotropy parameter. In a spherical system we compare the motions of the stars in radial direction to the motions in spherical shells (tangential direction) at the given distance of the star. The velocity dispersions of motions are described by Equation (1). To quantify the anisotropy of the system we use the anisotropy parameter  $\beta$

$$\beta(r) \equiv 1 - \frac{\sigma_\theta^2(r) + \sigma_\phi^2(r)}{2\sigma_r^2(r)} \quad (2)$$

taken from Binney and Tremaine (2008, eq. 4.61). The numerator describes the velocity dispersion on the spherical shell while the denominator is given by the squared radial

dispersion. If  $\beta$  is positive the anisotropy is radial i.e. the velocity dispersion is larger in radial direction than in tangential direction, if it is negative the anisotropy is tangential and if  $\beta \approx 0$  then the system is isotropic, that means the stars have random motions in all directions at the same rate.

## 2.3 Density and potential

### 2.3.1 Density of a collisionless stellar system

GCs are classical examples for quasi-collisional stellar systems, i.e. the motions are dominated by two-body interactions. To allow for an investigation of the orbits the stars are *currently* on, we assume that a star only feels the gravitational forces generated by a smooth overall stellar density distribution, i.e. we assume the system to be collisionless at the moment of our investigation. This is approximately motivated by the fact that the dynamical time of a cluster is always shorter than the relaxation time  $T_{\text{dyn}} < T_{\text{relax}} < T_{\text{ageGC}} \equiv T_{\text{Hubble}}$ .  $T_{\text{dyn}}$  is approximated by the time of a star to go from one side of the cluster to the other. This takes approximately  $10^5$  yr. The relaxation time is the time needed to redistribute energies of the stellar encounters and takes about  $10^7 - 10^9$  yr. The age of the GCs is approximately the Hubble time which is the age of the universe ( $10^{10}$  yr).  $T_{\text{dyn}} < T_{\text{relax}}$  motivates the collisionless approximation while  $tT_{\text{relax}} < T_{\text{ageGC}} \equiv T_{\text{Hubble}}$  is telling us that a GC has lived for several relaxation times, therefore two-body interaction had time to act. That means that the system is collisional in the long term, see also Binney and Tremaine (2008, p.555) and Williams *et al.* (2012).

We calculate the mass density of the GCs by binning the masses on logarithmic equally distributed shells with shell boundaries at  $r'_i$

$$\rho_i = \frac{\sum_k M_k}{V(r'_{i+1} - r'_i)} = \frac{3}{4\pi} \frac{\sum_k M_k}{r'_{i+1}^3 - r'_i^3} \quad (3)$$

with the mass  $m_k$  of k-th star, at radius  $r_k$  where  $r'_i = r_k = r'_{i+1}$  over a volume  $V$  which is taken from the radius of the inner shell  $r'_i$  and the radius of the outer shell  $r'_{i+1}$ . We set  $\rho_i \equiv \rho(r_i)$  with  $r_i$  as mean of all  $r_k$ .

### 2.3.2 Generating the potential from Poisson's equation

If the system is spherical symmetric the potential and force depend only on the distance from the centre  $r$ . Under the condition that the system is collisionless, the potential  $\Phi$

can be derived from the Poisson's equation

$$\Delta\Phi(r) = 4\pi G\rho(r) \quad (4)$$

with the gravitational constant  $G = 6.674 \cdot 10^{-11} \text{ m}^3/\text{kg s}^2$  (Mohr *et al.*, 2015) and the density  $\rho$  depending only on the distance to the centre as well. In general, one can use the Poisson's equation for every system but then it is depending on the position vector  $\vec{x}$ .

Due to the spherical symmetry the potential can be calculated by

$$\Phi(r) = -\frac{G}{r} \int_0^r dM(r') - G \int_r^\infty \frac{dM(r')}{r'} = -4\pi G \left[ \frac{1}{r} \int_0^r dr' r'^2 \rho(r') + \int_r^\infty dr' r' \rho(r') \right] \quad (5)$$

with  $dM$  describing the mass of spherical shells as proved by Binney and Tremaine (2008, eq. 2.28).

To numerically calculate the integrals of Equation (5) from the interpolated density in Section 2.3.1 we use the Gauss-Legendre quadrature

$$\int_a^b f(x)dx \approx \frac{b-a}{2} \sum_{i=1}^n w_i f \left( \frac{b-a}{2}x_i + \frac{a+b}{2} \right) \quad (6)$$

where the points  $x_i$  and the weights  $w_i$  are derived from the Legendre polynomials and  $a$  and  $b$  are the integration limits. This gives us the numerical formula for the potential

$$\begin{aligned} \Phi(r) = & -4\pi G \cdot \frac{1}{2} \sum_{i=1}^n w_i \left( \frac{r}{2}x_i + \frac{r}{2} \right)^2 \rho \left( \frac{r}{2}x_i + \frac{r}{2} \right) \\ & -4\pi G \cdot \frac{\infty-r}{2} \sum_{i=1}^n w_i \left( \frac{\infty-r}{2}x_i + \frac{\infty+r}{2} \right) \rho \left( \frac{\infty-r}{2}x_i + \frac{\infty+r}{2} \right) \end{aligned} \quad (7)$$

### 2.3.3 Other potential models

One of the most simple potentials is the Kepler potential. It describes the potential given by a point mass  $M$

$$\Phi(r) = -\frac{GM}{r} \quad (8)$$

taken from Binney and Tremaine (2008, eq. 2.34). The potential generated by the IMBHs can be described as Keplerian.

Another description of spherical systems is given by the Plummer model. It is based on the assumption that the density is nearly constant in the centre and equals zero at

large radii. The given potential is

$$\Phi(r) = -\frac{GM}{\sqrt{r^2 + b^2}} \quad (9)$$

(Binney and Tremaine, 2008, eq. 2.44a) where  $M$  is the total mass of the system and  $b$  is the Plummer scale length. In Plummer (1911) this potential is used to describe observations of GCs. The corresponding density to this model is given by Binney and Tremaine (2008, eq. 2.44b)

$$\rho(r) = \frac{3M}{4\pi b^3} \left(1 + \frac{r^2}{b^2}\right)^{-\frac{5}{2}}. \quad (10)$$

Another potential, which is the most general potential for which the actions (see Section 2.4.3) can be calculated exactly and analytically without the use of an integration, is the isochrone potential

$$\Phi(r) = -\frac{GM}{b + \sqrt{b^2 + r^2}} \quad (11)$$

(Binney and Tremaine, 2008, eq. 2.47). The Kepler potential is a special case of the isochrone potential with  $b=0$ .

## 2.4 Orbits and integrals of motion

### 2.4.1 Classical integrals of motion in spherical potentials

If a tracer particle, e.g. a star, moves freely in a gravitational potential generated by a mass distribution its path in 6D position-velocity space  $(\vec{x}(t), \vec{v}(t))$  is called "orbit". The way in which positions and velocities along the orbit are linked contains information about the potential. With Newton's 2nd law we get the connection between potential  $\Phi(\vec{x})$  and acceleration  $\vec{a}(\vec{x})$  which the star of mass  $m$  experiences which is

$$\vec{F}(\vec{x}) = -m\nabla\Phi(\vec{x}) = m \cdot \vec{a}(\vec{x}). \quad (12)$$

Here  $\vec{F}$  is the force at given position  $\vec{x}$ .

Beside the description of orbits in the 6D position velocity space, orbits can be described by integrals of motion which are constant along an unperturbed orbit. A spherical potential allows four conserved quantities, e.g. the classical integrals of motions, which are the energy and the three components of the angular momentum. That restricts the orbits in spherical potentials to lie in a plane. The (specific) energy is given

by the sum of the kinetic energies in the 3D velocity space and the potential energy:

$$E(r) = \frac{v_x(r)^2 + v_y(r)^2 + v_z(r)^2}{2} + \Phi(r). \quad (13)$$

The total (specific) angular momentum

$$\vec{L} = \vec{x} \times \vec{v} = \sqrt{L_x^2 + L_y^2 + L_z^2} \quad (14)$$

can be written as superposition of the angular momenta in each direction which are given by

$$L_k = \epsilon_{klm} x_l v_m \quad (15)$$

where  $\epsilon_{klm}$  is the Levi-Civita symbol.

If an orbit is perturbed its integrals of motion can vary and evolve a time dependency. There are physical reasons for perturbations (e.g. scattering due to two- and three-body interactions when passing by other stars, stellar binaries or the IMBH); in computer simulations there can be in addition also numerical fluctuations of the orbits close to the IMBH. We assume that the stars move along unperturbed orbits.

#### 2.4.2 The effective potential

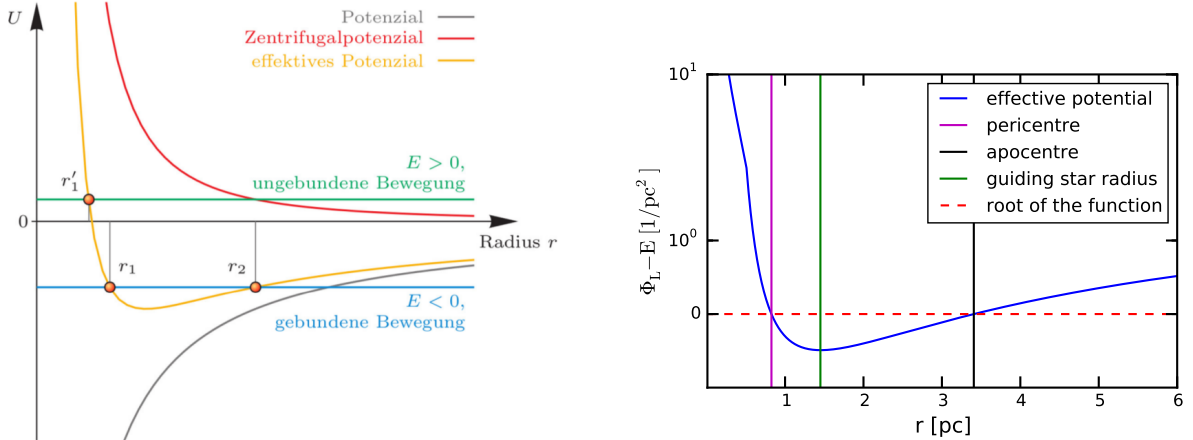
The effective potential  $\Phi_L(r)$  (see Figure 3) combines the effects of gravitational force and centrifugal force acting on a star moving with given angular momentum  $L$  in a gravitational potential  $\Phi(r)$ :

$$\Phi_L(r) = \Phi(r) + \frac{L^2}{2r^2}. \quad (16)$$

which is dependent on the centrifugal potential  $L^2/2r^2$  (taken from Bartelmann, 2007, p. 59, eq. 6.27). The centrifugal potential describes the energy that star has due to its rotation. If the orbit is unbound its total energy is larger than its effective potential at large radii. A star on a bound orbit has a total energy which is smaller than the effective potential everywhere except between a certain minimum and maximum radius.

These radii where the bound orbit has the smallest and respectively the highest distance to the gravitational centre are called pericentre  $r_{\min}$  and apocentre  $r_{\max}$ . There the effective potential equals the total energy  $E$  since the stars do not have any kinetic energy in radial direction. That results in the following function (see Figure 3b) which is to solve:

$$\Phi(r_0) - E + \frac{L^2}{2r_0^2} = 0 \Rightarrow \left(\frac{1}{r_0}\right)^2 + \frac{2 \cdot (\Phi(r_0) - E)}{L^2} = 0. \quad (17)$$



(a) General potential of a central field. The black line is the gravitational potential, the effective potential is given by the yellow line and the centrifugal potential by the red line. If the effective potential is positive the object is unbound while having a negative potential the object moves on a bound orbit. The points where the effective potential equals the total energy are the peri- and apocentre ( $r_1$  and  $r_2$ ) of the orbit. The point with the lowest effective potential is the guiding-star radius. This is the distance a star with given angular momentum would have on a circular orbit. (Bartelmann, 2007, p.59)

(b) Determination of pericentre, apocentre and guiding-star radius given by Equation (17). Where the difference between effective radius and total energy is zero (red dashed line), are the peri- and the apocentre of the star (magenta and black lines) and the minimum of the effective potential (green line) is the guiding-star radius. This figure shows function 17 for a star in SIM 1 (see Section 3.1) with energy  $E = -2.7 \times 10^{-25} \text{ pc}^2/\text{s}^2$  and total angular momentum  $|L| = 5.6 \times 10^{-13} \text{ pc}^2/\text{s}$ .

Figure 3: Effective potential (Panel (a)) and its root to calculate pericentre, apocentre and guiding-star radius (Panel (b)).

$r_0$  is the solution for peri- and apocentre.

The guiding-star radius is the distance at which a star with given total angular momentum would have a circular orbit. This is at the minimum of the effective potential. To get  $r_g$  we have to solve

$$\frac{\partial \Phi_L}{\partial r} = \frac{\partial \Phi}{\partial r} - \frac{L^2}{r^3} = 0 \Rightarrow r \sqrt{r \frac{\partial \Phi}{\partial r}} - |L| = 0 \quad (18)$$

where  $\sqrt{r \frac{\partial \Phi}{\partial r}} = v_{\text{circ}}(r)$  is the circular velocity. The guiding-star distance is an estimation for the radius where the star is on average. Therefore it can be used to have a better comparison of the positions of the stars in the different simulations since in the snapshots the stars are at a random position on their orbit.

### 2.4.3 Actions

In Section 2.4.1 we introduced the classical integrals of motion. Now we introduce actions which are the best choice of values to describe orbits. Like the classical integrals of motion they are constant over time and orbit. We can combine actions with angle coordinates. The angle coordinates evolve linearly in time while the star moves along the orbit and the actions are the corresponding conjugate momenta. Actions  $\vec{J}$  and angles  $\vec{\theta}$  form a set of 6D canonical conjugate coordinates. That means that the transformation from configuration space  $(\vec{x}(t), \vec{v}(t))$  to action-angle space conserves the phase space volume (i.e. the Jacobian determinant of the transformation is 1). Another reason to have them as best choice is that they have an intuitive physical meaning. They quantify the amount of oscillation along an orbit in the i-direction. Generally they can be calculated by

$$J_i \equiv \frac{1}{2\pi} \oint_{\text{orbit}} p_i \cdot dq_i \quad (19)$$

with the spatial coordinate in i-direction  $q_i$  and the corresponding canonical conjugate momentum  $p_i$  (if  $p_i$  is given per unit mass, i.e. is equal to the velocity  $v_i$ , then the radial action is given per unit mass as well).

For most potentials actions cannot be calculated analytically but in spherically symmetric potentials they can be described by relatively straightforward functions. The azimuthal action  $J_\phi$  and the latitudinal action  $J_\theta$  can be evaluated simply. To calculate the radial action  $J_r$  we have to solve an integral numerically. Actions of a spherical

potential are found to be

$$J_\phi = L_z, \quad (20)$$

$$J_\theta = L - |L_z|, \quad (21)$$

$$J_r = \frac{1}{\pi} \int_{r_{\min}}^{r_{\max}} dr \sqrt{2E - 2\Phi(r) - \frac{L^2}{r^2}} \quad (22)$$

(Binney and Tremaine, 2008, p. 221). The azimuthal action is given by the z-component of the angular momentum which is perpendicular to the  $z=0$  plane, i.e. it describes the amount of rotation around the z-axis. The latitudinal action is described by the angular momentum without the component in z-direction. It describes the amount of movement the star performs perpendicular to the  $z=0$  plane. The radial action is depending on pericentre and apocentre of the orbit as well as the potential, the total energy and the angular momentum of the orbit. If the radial action is large, then the orbit is either very eccentric and therefore  $r_{\max} \gg r_{\min}$  or it has a large radial velocity since the integrand equals the radial velocity, as explained in the following. An orbit with  $J_r = 0$  is circular since  $r_{\max} = r_{\min}$  and  $v_r = 0$ .

We give an heuristic explanation of the formula of the radial action. In the general equation to calculate actions, Equation (19), we set  $p_r = v_r$ , i.e. the velocity in radial direction. We can assume that the spatial coordinate is pointing in r-direction and therefore  $q_r = r$ . In a spherical potential the motions in  $r, \theta, \phi$ -direction are separable (Binney and Tremaine, 2008, sec. 3.5.2). That allows us to consider the integral in Equation (19) (for  $i=r$ ) independent of  $\vartheta$  and  $\phi$  so that the integral over the whole orbit reduces to a single integration from peri- to apocentre, because the orbit is a closed curve. This leads us to

$$J_r = \frac{2}{2\pi} \int_{r_{\min}}^{r_{\max}} v_r(r) dr. \quad (23)$$

Now we consider the motion in orbital plane only. We can separate it into the radial motion with given radius  $r$  and corresponding velocity  $v_r$  and into tangential motion with given angle  $\vartheta$  and velocity  $v_\vartheta$ . The kinetic energy can then be described as the sum of kinetic energy in radial direction  $E_r$  and in angular direction  $E_\vartheta$  which is the rotation

energy:

$$E_{\text{kin}} = E_r + E_\vartheta, \quad (24)$$

$$E_r \sim \frac{v_r^2}{2}, \quad (25)$$

$$E_\vartheta \sim \frac{v_\vartheta^2}{2} \sim \frac{L^2}{2r^2}. \quad (26)$$

We can write the radial energy as sum of the other energies and derive the radial velocity from that:

$$\begin{aligned} E &= E_{\text{kin}} + \Phi(r) \\ \implies E_r &\sim E - \Phi(r) - \frac{L^2}{2r^2} \\ \Leftrightarrow \frac{v_r^2}{2} &\sim E - \Phi(r) - \frac{L^2}{2r^2} \\ \implies v_r &\sim \sqrt{2E - 2\Phi(r) - \frac{L^2}{r^2}}. \end{aligned}$$

We can set this result in the integrand of Equation (23) which gives us the equation of the radial action.

For the isochrone potential in Equation (11) the radial action given by Equation (22) reduces to the simple expression

$$J_r = \frac{GM}{\sqrt{-2E}} - \frac{1}{2} \left( L + \sqrt{L^2 + 4GMb} \right) \quad (27)$$

(Binney and Tremaine, 2008, p.221, eq. 3.225).

#### 2.4.4 Numerical orbit integration

To describe the orbit of a star in a potential we need the position and velocity at each time step. For general potentials this has to be calculated numerically. We use the numerical leapfrog method which is a second-order accurate, time reversible, symplectic integrator (Binney and Tremaine, 2008, p.199/200). Second-order accurate means that the error of the position after one timestep  $\Delta t$  is proportional to the 3rd power of the timestep and symplectic means that it conserves the volume of the phase space. This integrator uses kick steps and drift steps. When doing a kick step the position stays the same and the momentum changes. When doing a drift step the position changes and

the momentum stays the same. One variant is the "drift-kick-drift" leapfrog where the steps are calculated as follows:

$$\vec{x}_{1/2} = \vec{x} + \frac{1}{2}\vec{v}\Delta t \quad ; \quad \vec{v}' = \vec{v} - \nabla\Phi(\vec{x}_{1/2})\Delta t \quad ; \quad \vec{x}' = \vec{x}_{1/2} + \frac{1}{2}\vec{v}'\Delta t \quad (28)$$

(adapted from Binney and Tremaine (2008, eq. 3.166a)). The second time derivative of  $\vec{x}(t)$  is the acceleration, which we can assume as constant for small enough timesteps. Integrating the acceleration gives us the velocity at given time  $t$  with constant values for the acceleration and velocity. Another integration leads to the position at time  $t$  with constant acceleration, velocity and position:  $\vec{x}(t) = \frac{1}{2}\vec{a}_0 t^2 + \vec{v}_0 t + \vec{x}_0$ . If we let this position at time  $t_i$  move for a timestep  $\Delta t$  then we get Equation (29). According to Equation (12) the potential is related to the acceleration by  $\nabla\Phi(\vec{x}) = -\vec{a}(\vec{x})$ . If the timestep  $\Delta t$  is small enough we can assume that the acceleration is constant for this step and that the acceleration of the half step can be described by the sum of half of the acceleration at the beginning of the step and half of the acceleration at the end of the step. That allows us the following substitution:  $-\nabla\Phi(\vec{x}_{i/2}) = \frac{\vec{a}(\vec{x}_{i+1}) + \vec{a}(\vec{x}_i)}{2}$  and leads us to Equation (30):

$$x_{i+1} = x_i + v_i \Delta t + \frac{a(x_i)}{2} \Delta t^2 \quad (29)$$

$$v_{i+1} = v_i + \frac{a(x_{i+1}) + a(x_i)}{2} \Delta t. \quad (30)$$

We have implemented the leapfrog integrator in the form of Equations (29) and (30) with Equations (28) as fundamental equations of this method.

Now we show some examples of different kind of integrated orbits by the leapfrog method in spherically symmetric potentials. We use an isochrone potential in which actions, especially the radial action can be calculated exactly and analytically, see Equations (20), (21) and (22). It is also an approximative description of GCs (Binney, 2014). It is calculated by Equation (11) using the best fit values of the total mass  $M$  and the scale length  $b$  from fitting the isochrone density profile to the density profile of one of our simulations, SIM 1 (see Section 3.1). The best fit parameters are  $M=1.3\times 10^5 M_\odot$  and  $b=0.54$  pc. To get the isochrone potential, integrate the orbits and get the integrals of motion we want to investigate we use galpy, a python package for galactic dynamics from Bovy, 2015. We have implemented this method as well, but use galpy due to its good stability, its faster runtime and its versatility.

All three orbits of Figure 4 move in a plane, because the angular momentum  $\vec{L}$  is

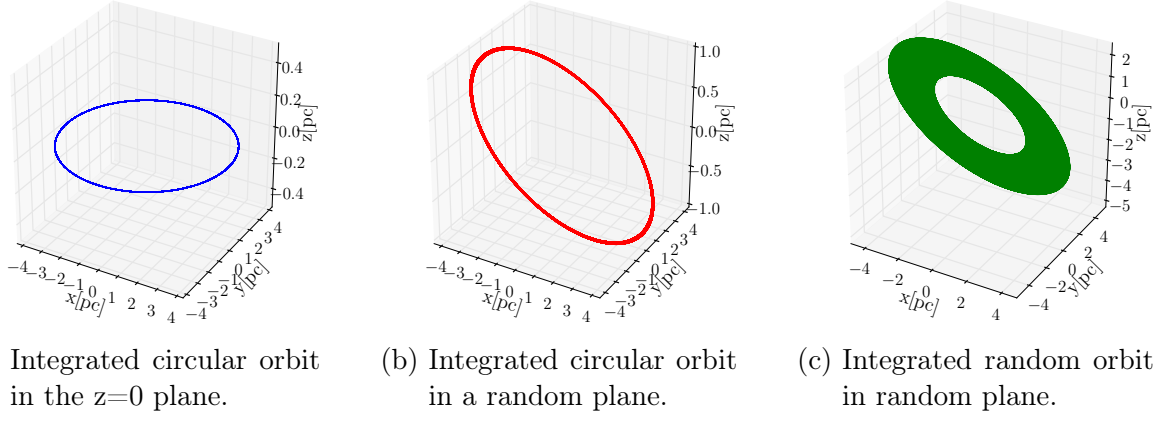


Figure 4: Three examples of orbits integrated with the leapfrog integrator using galpy. The initial conditions are given in Table 1.

conserved. For a long enough integration time the orbit completely fills the annulus between its pericentre and apocentre. The orbit in Panel (c) has a radial action  $J_r > 0$  (see Figure 4). The circular orbits in Panels (a) and (c) have no inward or outward motion and  $J_r = 0$ . In Panel (b) the plane of the orbit is rotated with respect to the  $z=0$  plane. We choose following initial conditions for position, velocity and therefore the radial action:

	$r$ [pc]	$z$ [pc]	$\phi$ [pc]	$v_r$ [pc]	$v_T$ [pc]	$v_z$ [pc]	$J_r$ pc km/s
Panel (a)	4.13	0.0	0.0	0.0	10.15	0.0	0.0
Panel (b)	4.13	-0.83	0.0	0.0	10.15	0.0	0.0
Panel (c)	4.13	-2.07	0.0	2.03	8.12	-2.03	0.85

Table 1: Overview of the initial conditions used for the orbit integration. All position coordinates are given in pc and the velocity coordinates are given in km/s. The radial action  $J_r$  is given in pc km/s. The radius is given by  $r$ , the height by  $z$  and the angular coordinate by  $\phi$ . The velocities are given by  $v_r$  in the radial direction and  $v_T$  and  $v_z$  as tangential velocities.

### 3 Analysis

In this section we analyse different aspects of the simulations. In Section 3.1 we describe the simulations, their underlying models and give an overview of their properties. The next step in Section 3.2 is to fit isochrones to the CMD to verify given age and metallicity. After that, we investigate the phase space in Section 3.3. We look for a rise in the velocity dispersions of the GCs with IMBH and examine the anisotropy parameters. Then we determine the density distribution, check for the sphericity of the systems and compute the potential starting from the density. From that, we "translate" the simulation into action space in Section 3.4. There we study the radial action versus different properties such as the guiding-star distance or the classical integrals of motion to see if we can find a signature of the presence of an IMBH.

#### 3.1 Description of the globular cluster simulations

We consider a set of Monte Carlo cluster simulations, developed with the Monte Carlo code MOCCA of Hypki and Giersz (2013) (see also Giersz 1998). The simulations include an initial mass function, stellar evolution, primordial binaries, and a relatively high number of particles, providing a realistic description of the long-term evolution of GCs with a single stellar population.

All the simulation have a metallicity of  $[Fe/H]=-1.3$  and a Kroupa (2001) initial mass function. The first simulation (from Giersz *et al.* 2015, kindly shared by the authors) contain an IMBH of  $10^4 M_{\odot}$  and its initial condition is drawn from a King model with concentration parameter  $W_0=6$ ,  $6.9 \times 10^5$  initial number of particles, 95 % of which are binary systems. We consider two snapshots of the simulation, one at 10 Gyr and one at 7 Gyr. We call these snapshots SIM1-IMBH and SIM2-IMBH, respectively. The other two simulations (from Downing *et al.* 2010, kindly shared by the authors) do not contain an IMBH and have an initial number of particles of  $5 \times 10^5$  and  $2 \times 10^6$ , 10 % of initial binaries, and initial conditions drawn from a Plummer (1911) model with a ratio between the initial tidal radius and half-mass radius of 75. We consider a 11 Gyr snapshot for both simulations and we call them SIM3-NOIMBH and SIM4-NOIMBH, respectively.

We summarize in Table 2 the properties of the simulations for the time-snapshots considered.

The output of the simulations relevant for our work are for each star: the position vector  $\vec{x}$ , the velocity vector  $\vec{v}$  in Cartesian and polar coordinates, mass, luminosity, magnitude B and V band and whether the star is a binary or not.

Name of the simulation	Number of particles	Total mass [ $M_{\odot}$ ]	Mass of theIMBH [ $M_{\odot}$ ]	$r_m$ [pc]	Age [Gyr]	Binary fraction [%]
SIM 1 - IMBH	1026735	$3.09 \times 10^5$	10102	4.13	10	7.5
SIM 2 - IMBH	1079376	$3.26 \times 10^5$	8902.3	3.58	7	7.8
SIM 3 - NOIMBH	468627	$1.73 \times 10^5$	0	7.89	11	3.0
SIM 4 - NOIMBH	1851556	$6.70 \times 10^5$	0	5.41	11	3.3

Table 2: Overview of the data of the simulations. We show the basic properties of each simulation which are number of particles, the total mass, the mass of the IMBH, the half-mass radius, the age and the binary fraction. The half-mass radius is defined by the radius which includes half of the mass of the whole system.

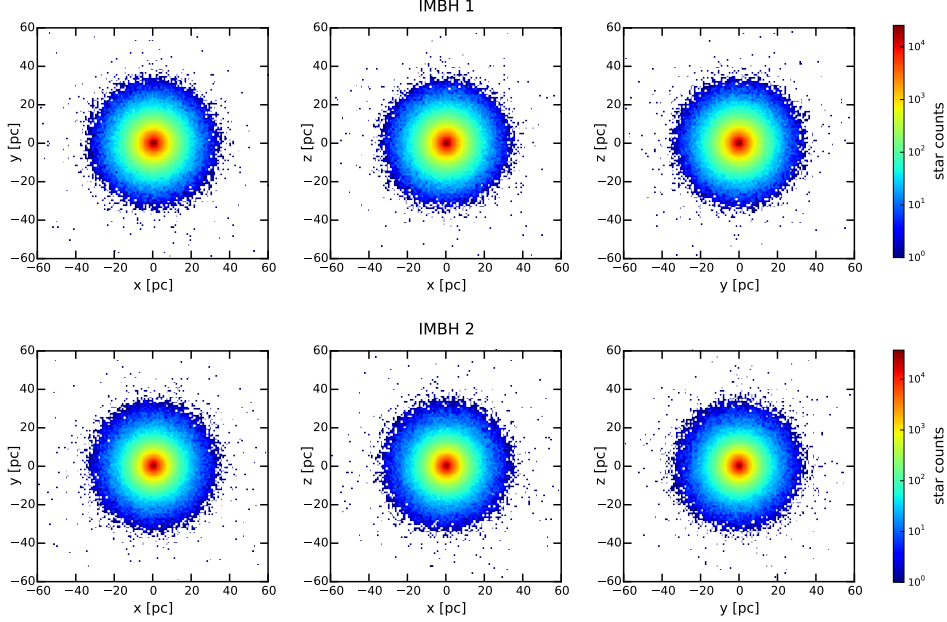
We compute the half-mass radius  $r_m$  given in Table 2 by calculating the distance where half of the mass of the GC is inside the sphere of given distance and half of the mass is distributed outside of this sphere. We need it to compare aspects of the different simulations especially in phase space investigations since their actual sizes are different for each simulation and, therefore, are not directly comparable. In action space we use the guiding-star radii (see Equation (18) in Section 2.4.2) as a typical radius characterising an orbit.

To get familiar with the simulations we first have a look at the spatial (see Figure 5) and the velocity distribution (see Figure 6) of the stars. We see that both simulations with IMBH have some stars and velocities out of the main sphere while these stars do not occur in the simulations without IMBH. This could be due to different initial conditions of the different simulations.

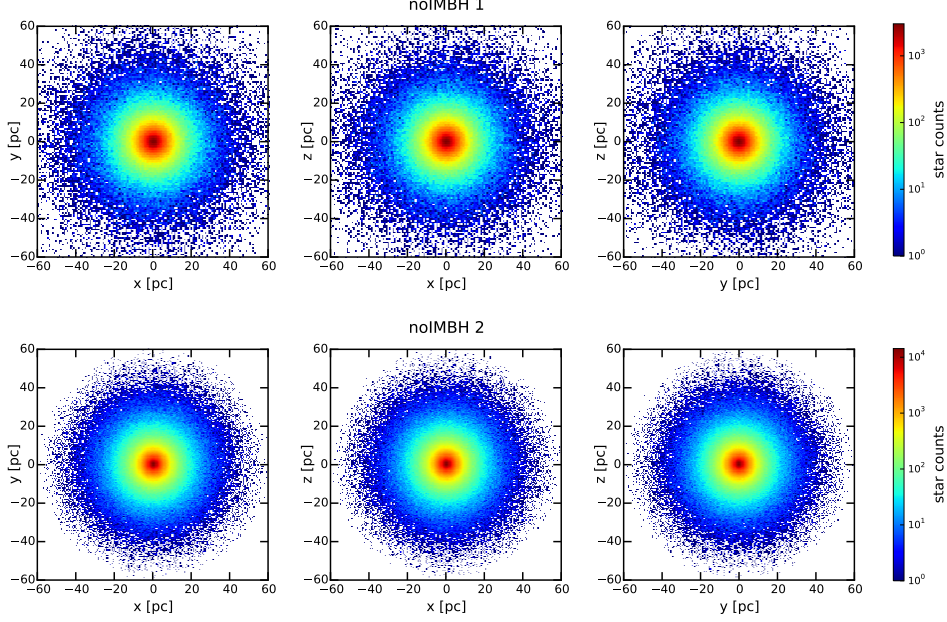
### 3.2 Investigation in color magnitude space

As mentioned in Section 2.1 the CMD shows the evolution stage of a star from its position on the diagram. If one does not know the age or metallicity of the system, isochrones (taken from and computed on the basis of Bressan *et al.* 2012) can be fitted on the CMD. Isochrones are curves of evolutionary stages of stars of a SSP having the same age and metallicity but different masses. In Figure 7 we plot several isochrones to our CMD to determine which one fits best. We used random compositions of ages and metallicities around the given values from SIM 1. The age of the isochrones ranges from 9 to 11 Gyr. The metallicity  $z$  is given by

$$[\text{Fe}/\text{H}] = \log \left( \frac{z}{z_{\odot}} \right) = -1.3 \quad (31)$$

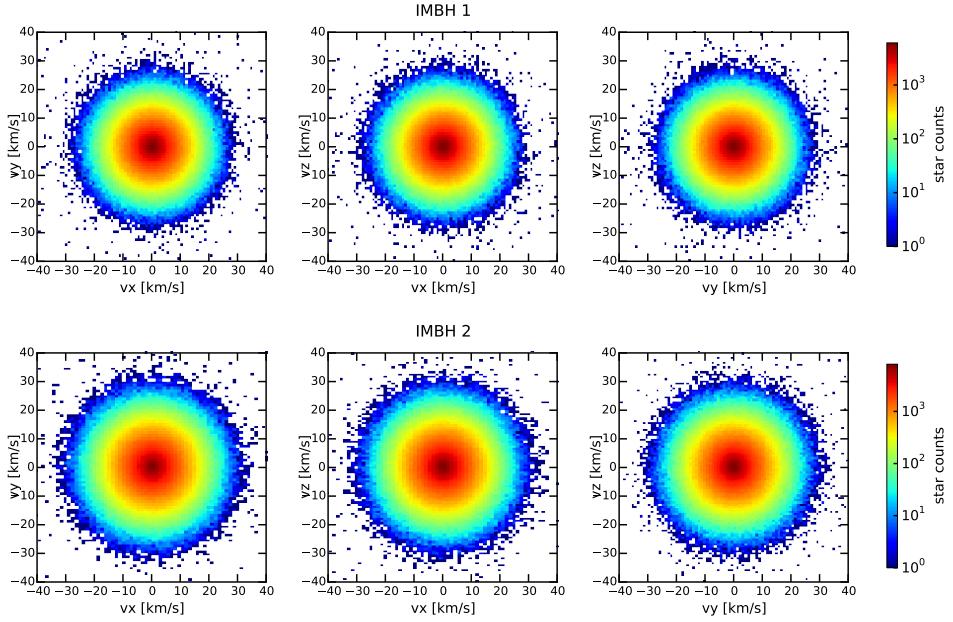


(a) SIM 1 & SIM 2. The GCs are spread until 100 pc with most of the stars located in the inner 40 pc.

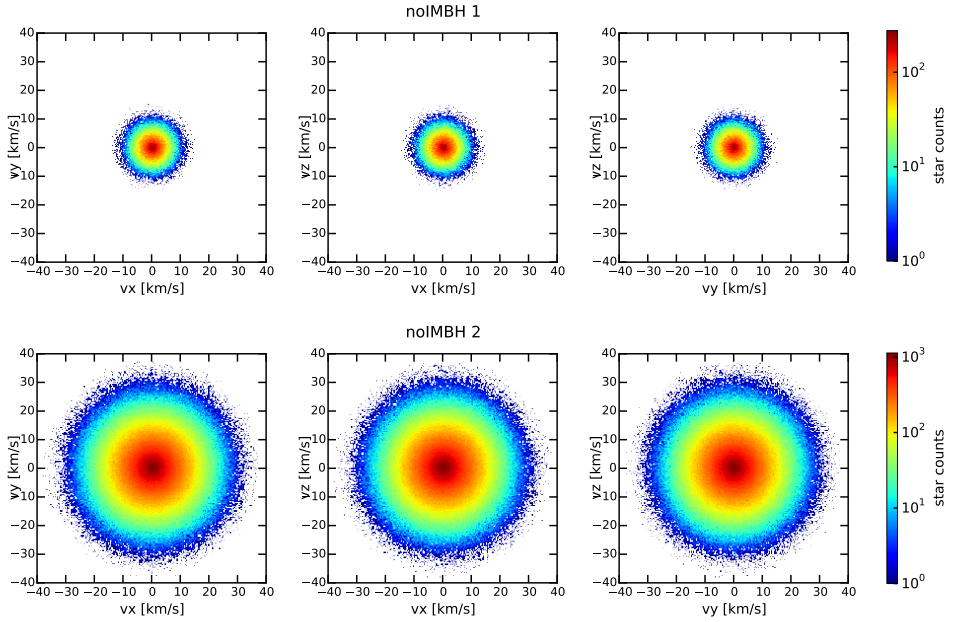


(b) SIM 3 & SIM 4. The GCs are spread until 90 pc (SIM3) and until 60 pc (SIM4).

Figure 5: Spatial distribution of stars in the simulated GCs. The stars are distributed spherically with most of the stars in the inner part. The stars of the GCs with IMBH are less spread in the outer parts except very few which are far outside. This is simply due to the different initial concentration conditions of the simulations. In the GCs without IMBH the stars in the outer part are less accumulated but the furthermost stars are still in the main sphere.



(a) SIM 1 & SIM 2. The velocities of the stars are spread until 120 km/s with most of them reaching 30 km/s.



(b) SIM 3 & SIM 4. The velocities of the stars are spread until 15 km/s for SIM 3 whereas they are spread until 40 km/s for SIM 4.

Figure 6: Velocity distribution of stars in the simulated GCs. The velocities are isotropically spread around  $\vec{v} = 0$ . Most of the stars have low or no velocity while a few have high velocities in different directions. There are no overall streaming motions.

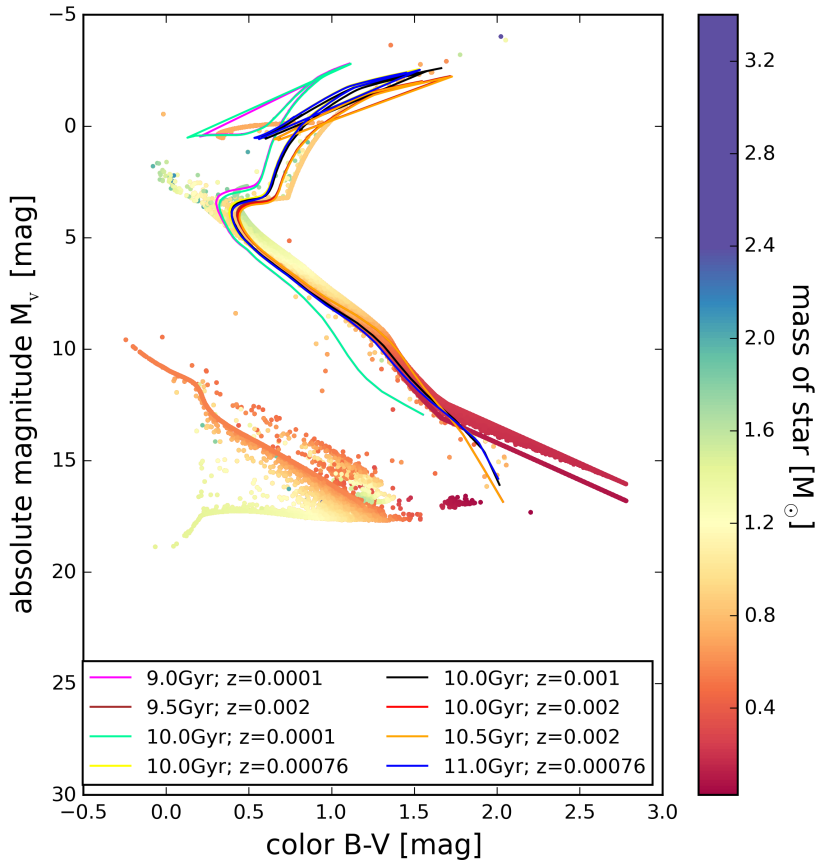


Figure 7: Color magnitude diagram of SIM 1 overplotted with different isochrones. The stars are color coded by their mass. The colorbar is given as in Figure 2. The ages and metallicities of the isochrones are chosen around the age and metallicity of SIM1. The black line represents the true values. We see that we cannot clearly get information about age and metallicity since the isochrones of different ages and metallicities are partly overlying but the isochrone with the true properties fits the CMD at least as well as the other isochrones.

where  $\text{Fe}/\text{H}$  is the fraction of iron to hydrogen and  $z_{\odot}$  ist the metallicity of the Sun. There are different values for  $z_{\odot}$ . In Marigo *et al.* (2008) it is given by  $z_{\odot} = 0.019$  which leads to  $z=0.001$  while in Bressan *et al.* (2012)  $z_{\odot} = 0.0152$  which gives us  $z=0.00076$ . The other both metallicities are randomly chose with  $z=0.0001$  and  $z=0.002$ . The best fitting isochrone gives us the age and the metallicity of the system. The black isochrone is the line given from SIM1. The age is best determined in the turn off point. We see that several isochrones fit the turn-off, only the isochrones with a metallicity of  $z=0.0001$  do not fit the turn-off. The isochrones with above calculated metallicities fit well the main sequence and the early asymptotic giant branch, but lack to fit the red giant branch, while the isochrones with higher metallicity ( $z=0.002$ ) fit the red giant branch better but they do not fit the main sequence very well. We cannot clearly choose one best fitting isochrone but we see that the black line with right age and metallicity is consistent with the simulation. The lines from the early asymptotic giant branch to the horizontal branch are not physically correct, they appear due to the sorting of the given information of the isochrones.

The stars in a GC are characterized by different stellar masses as shown from the color-code of Figure 7. The evolved stars (red giants, horizontal branch stars, asymptotic giants) are characterized by a mass of  $\approx 0.8 - 0.9 M_{\odot}$  while the main sequence stars have masses from  $\approx 0.8 - 0.9 M_{\odot}$  (at the turn-off) down to  $0.1 M_{\odot}$  at the faint end. Having a mass spectrum is important for the long-term dynamical evolution of a GC and gives rise to the phenomena of mass-segregation and energy equipartition. Energy equipartition assumes that the stars of a system tend to have equal energies, but practical only partial energy equipartition is reached. This leads to mass segregation. High mass stars lose energy and therefore fall in the centre of the cluster while low mass stars gain kinetic energy and migrate towards the outer regions of the GC (Trenti and van der Marel, 2013). Throughout the following investigations we do not consider the mass dependence induced by energy equipartition and do not make a distinction for stars with different masses.

### 3.3 Investigation in phase space

First we investigate the GC in phase space for the set of simulations that we use throughout this work. We start with the tests of sphericity, origin and rotation to confirm that we can apply related assumptions. Then we show velocity dispersions and the anisotropy parameters and then the density profiles and from that get the potentials.

### 3.3.1 Testing for sphericity, origin and rotation

For SIM 1 we test the sphericity of the GC and its centre of mass (COM) and for all simulations the mean velocities in polar coordinates. Sphericity allows the usage of analytical methods that are very straight forward, especially for determining the potential of the globular cluster and from that, the actions in action space. The COM is being tested to see if we can assume the origin of the coordinate system as centre of the GC or if we have to consider another centre. The mean velocities are tested to see if the GC rotates, in this case, they would show some systematic trend. If there is no rotation the mean velocities should be distributed around zero.

We will test the sphericity and the COM in one step by splitting the GC into octants along the coordinate axes and compare their mass density profiles. This is done first for the centre of the coordinate system. We do the same for the COM,  $R$ , which is calculated by formula  $R = \frac{1}{M} \sum_{i=1}^n m_i r_i$  with  $M$  as total mass of the system and  $r_i$  and  $m_i$  radius and mass of the  $i$ -th star. We combine the test of sphericity and the test of the COM in Figure 8. The round symbols represent the density profiles with respect

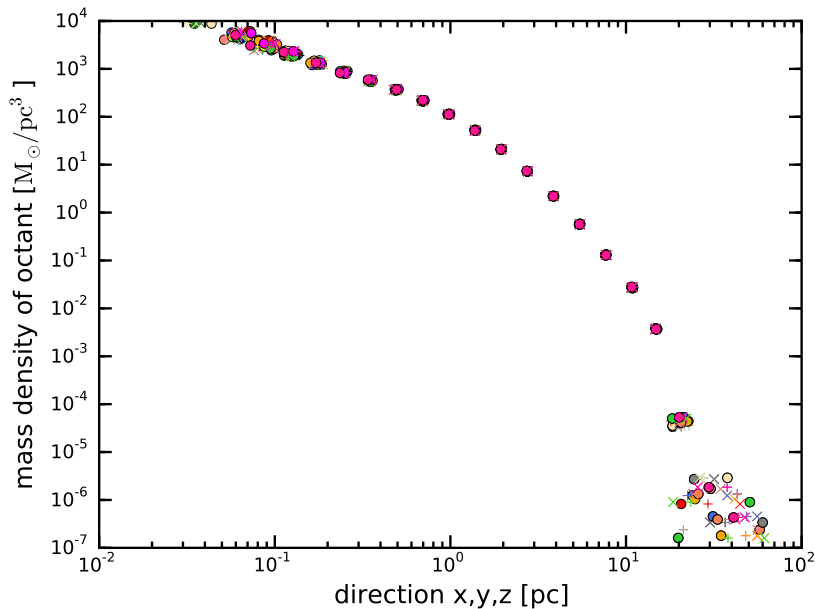


Figure 8: Test for sphericity and centre of mass of SIM 1. The mass density is plotted versus the distance in x, y and z direction. The sphericity tests for both origins are plotted. The origin of the coordinate system is described by the round symbol while the 'x'-symbol describes the COM. Each octant has its own color but the same octants of both sphericity tests have the same color.

to the origin of the coordinate system while the 'x'-symbols represent the profiles with

respect to the COM. The different colors represent each octant. For both tests we use the same colors for the same octants. Until the furthermost bin the density profiles for the different octants are consistent with each other. In the last bin the stars are binned over a wide distance and mass range. Since we calculate the mean distance, the scatter of the points is higher in the outer region, where we have low number statistics. Since all the profiles align we proved that the system is spherical symmetric and that we can choose the centre of coordinates as origin.

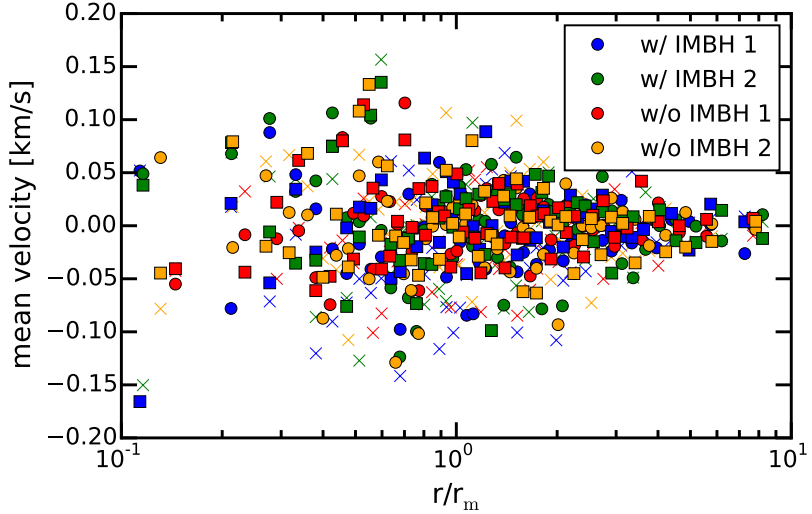


Figure 9: Test for inner rotation in the GCs. Each color represent one simulations (see also Figure 10) and each symbol represent the velocity in a certain direction. 'x' represents the radial velocities, the round symbols the azimuthal velocities and the squares the polar velocities. They are equally spread around zero in every direction for all GCs.

In Figure 9, we test the mean velocity and therefore the rotation of the system. We plot the mean velocity of every bin against the mean distance of the bin for the velocities in each direction of all GCs. If we had rotation we would get velocities that are significantly non-zero in the azimuthal and the polar velocities. If we had a bulk motion outwards or inwards we would get non-zero radial velocities. Since the mean velocities are equally distributed around zero none of the GCs rotates, as expected from the initial conditions of the simulations.

### 3.3.2 Kinematics

With Equation (1) from Section 2.2 we can calculate the velocity dispersion in each coordinate direction  $\sigma_r, \sigma_\theta, \sigma_\phi$ . For every bin we take the same amount of stars and

calculate the dispersion along the radius of the GC. As radial values we use the average radius of the stars falling in the bins. To compare all simulations we plot the dispersion over the distance in units of the half-mass radius. The half-mass radii of the simulations can be taken from Table 2. As expected, in Figure 10 we see a rise in the centre for the simulations with IMBH. This is due the high gravitational potential of the IMBHs which disturbs the dynamics of close stars. The rise is equally visible in all three velocity components. This is since the kinematics are isotropic in the centre of the GC (see Figure 11). There is no difference in the polar (Figure 10c) and the azimuthal (Figure 10b) velocity dispersion profiles because the system is spherical symmetric. In the outer regions the radial velocity dispersion, see Figure 10a, decreases less rapidly than for tangential velocity dispersions. The motion in the outer angular shells seems to be different to the motion in radial direction.

In Figure 10 we note a difference in the radial and in the tangential velocity dispersion. To properly quantify that difference we consider the anisotropy profile in Figure 11. Anisotropy can be calculated from Equation (2) given in Section 2.2. Radial anisotropy means that there is higher velocity dispersion in radial direction than in angular direction. This comes probably along with a substantial number on eccentric orbits. The profile is binned the same way as the velocity dispersions and given in units of the half-mass radius. In the central  $\approx 2 r_m$  of all GCs there is almost the same anisotropy: isotropy in the centre and radial anisotropy while going in the outer parts. That means that the systems are radial anisotropic. In the centre, the anisotropy is zero. There the system is isotropic and the stars move in no preferred direction. The GCs with IMBH are most radially anisotropic at about 4 half-mass radii. The other GCs are becoming more radial anisotropic the further away from the centre it is. The difference is due to different truncation prescriptions of the simulations.

### 3.3.3 Spatial distribution

It is important to determine the density distribution for several reasons:

- We want to compare the radial density profiles of the simulated GCs to see if they are similar to each other
- and if they can be described by classical GCs profiles like the Plummer potential (see Section 2.3.3).
- Can we maybe already determine a signature of the IMBH in the density distributions?

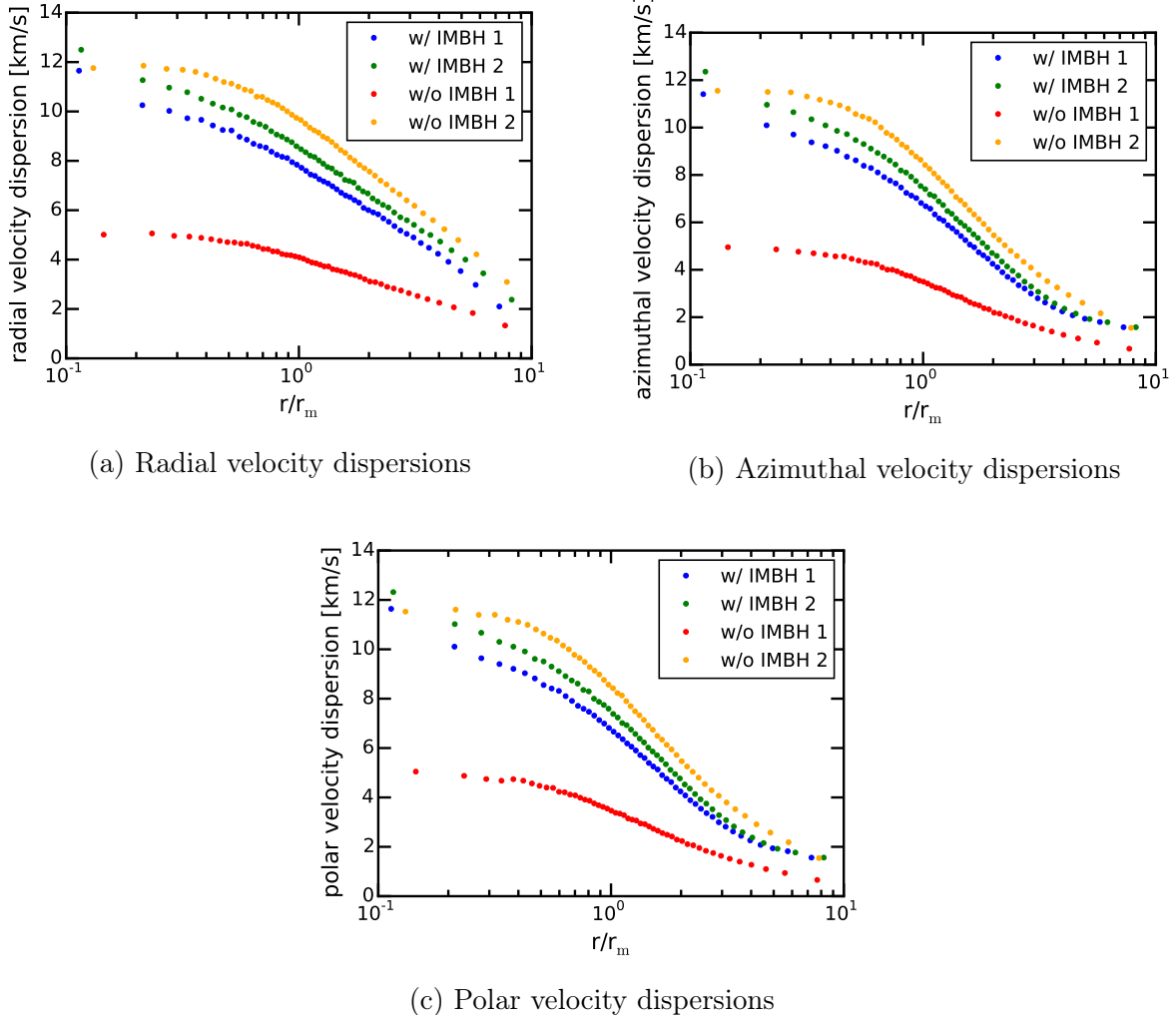


Figure 10: Velocity dispersion profiles of  $v_r$ ,  $v_\phi$ ,  $v_\theta$  as a function of the radius in units of the half-mass radius  $r_m$ . Blue and green points are the velocity dispersions of SIM 1 and 2 corresponding w/ IMBH 1 and w/ IMBH 2 and the red and yellow ones are the velocity dispersions of SIM 3 and 4, corresponding w/o IMBH 1 and w/o IMBH 2. They are binned in a way that each bin contains the same amount of stars. The given radius is the mean radius of the stars of each bin. We can see that the velocity dispersion of the simulations with IMBH rises towards the centre whereas the simulations without IMBH exhibits a cored profile.

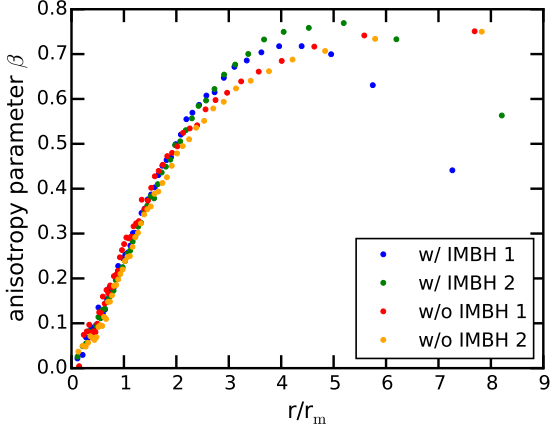


Figure 11: Profile of the anisotropy parameter  $\beta$  (see Section 2.2 for definition). The colors are given as in Figure 10. All simulations are isotropic in the centre and become increasingly radial anisotropic in the intermediate regions. The simulations with IMBHs have a peak at 4 and 5 half-mass radii where they are most radial anisotropic. Some difference in anisotropy is observable between the simulations with and without IMBH. This is due to different truncation prescriptions used in the simulations. We note that within  $\approx 2 r_m$  all simulations exhibit the same anisotropy profile.

- As mentioned in Section 2.3.2 we need the density profile to generate the overall gravitational potential of the GCs stellar distribution.

The density profile in Figure 12 shows the density calculated by Equation (3) of the system over its radius. As bins, we use radial shells with logarithmic spacing chosen so that there are at least 100 stars per bin to avoid low-number statistic.

In Figure 12a we see that SIM 1 and SIM 2 have very similar density profiles. SIM 1 has a slightly lower density since it lost about 5 % of its stars in between the snapshots and we do not include the IMBH in this profile which gained about 13 % mass. In the intermediate part of the GCs SIM 4 shows a similar density to SIM 1 and SIM 2. SIM 3 has a much smaller density than the other simulations. In Table 2 we see that SIM 3 has half of the stars of SIM 1 and SIM 2 which explains the difference. We also see that SIM 4 has double the amount of stars and double total mass than the GCs with IMBH. Still, the density plots are similar since we plotted them with the distance in units of the half-mass radius which is smaller for SIM 1 and SIM 2. If plotted over actual distance we would see that the density of SIM 4 is higher in the outer parts of the GC. In the central parts SIM 1 and SIM 2 are clearly rising which could be another signature of the IMBH while SIM 3 and SIM 4 show a cored profile despite the innermost point of SIM

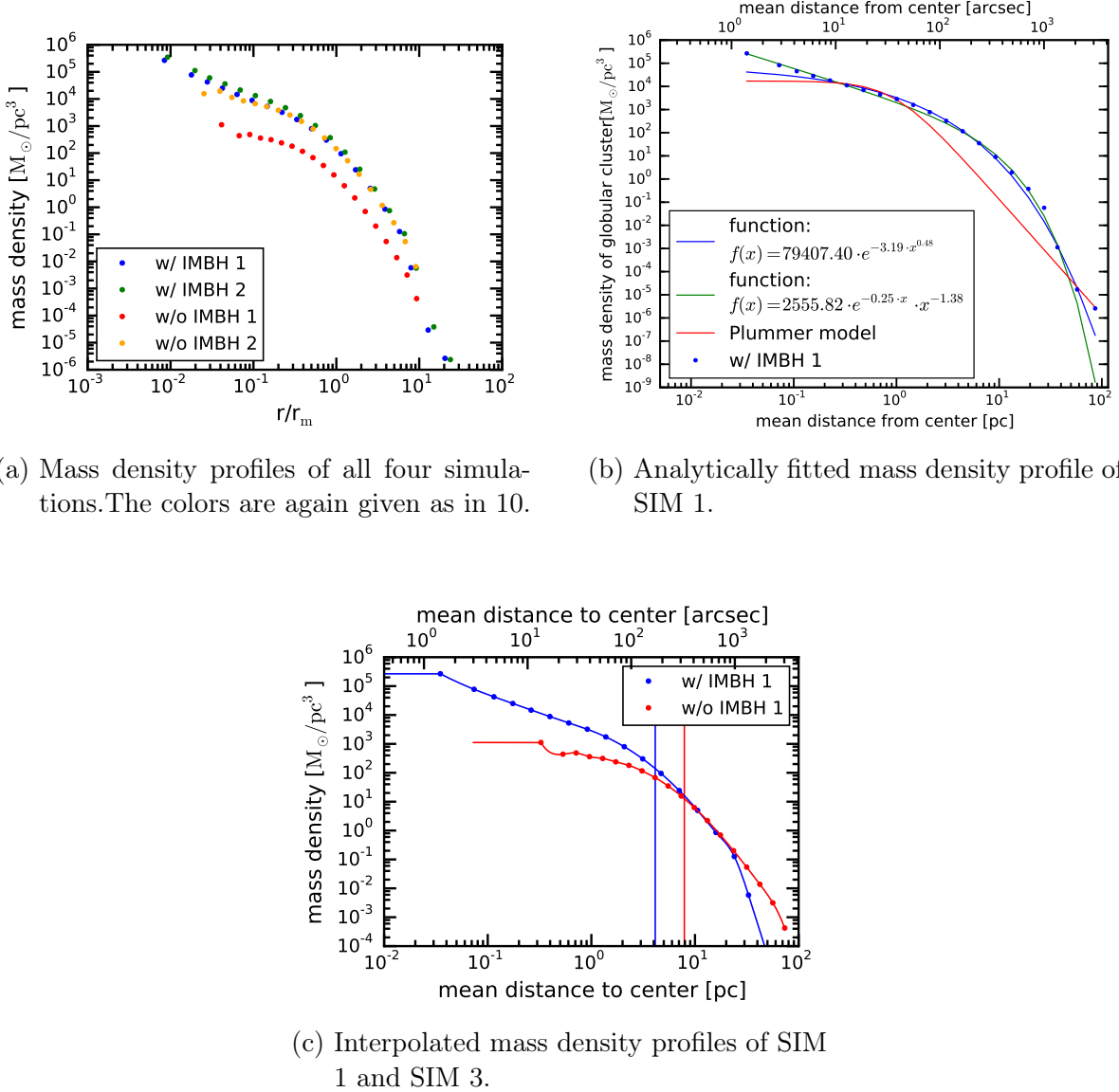


Figure 12: Stellar mass density profiles. Colors and labels of the different simulations are given as in Figure 10. The density in  $M_{\odot}/pc^3$  is plotted versus the radius in units of the half-mass radius in Panel (a). In Panel (b) there are two analytical functions and the Plummer model fitted to the density of SIM 1. Panel (c) shows the interpolation of SIM 1 and SIM 3 with their half-mass radii as vertical line. The densities of the GCs with IMBH is similar to SIM 4 and higher than the density of SIM 3. In the centre, there is a raise in the density of the GCs with IMBH whereas the other GCs stay approximately on the same level with a cored profile despite the innermost point of SIM 3. We can see in Panel (b) that it is not simple to find an analytical function or model describing the density globally for both small and large radii. That is why we interpolate it in Panel (c). Everything out of the GC is set to zero while the innermost density is set to be the value of the innermost point. The analytical interpolation is needed in the end of this section to calculate the potential given by the density.

3. In the furthermost regions the densities of SIM 3 and SIM 4 fall very steeply, while SIM 1 and SIM 2 flatten a little bit.

We try to find an analytic fitting function to the density profile in Figure 12b. This is essential for then calculating the potential from the Poisson's Equation (4) and to carrying out our following analysis. We use two variations of an exponential function,  $f_1(x) = a \cdot e^{x^c}$  and  $f_2(x) = a \cdot e^x \cdot x^c$ , and tried to fit them to the profile. The first function does not fit well the inner part while the second function does not describe the density in the outer parts. Also we want to check if the density follows a classical GC profile like, for example, the Plummer profile (see Equation 10 in Section 2.3.3). This one is much worse than the exponential functions. We see that we cannot find a simple fitting function nor a classical profile which describes the density throughout its radial extent.

To still be able to get a numerical handle on the density profile we will use the interpolated density in  $\log \rho$  versus  $\log r$  given in Figure 12c. To have an interpolation independent of the behaviour of the interpolation before the first and after the last bin we set the values there as fixed values. Outside of the cluster the density is set to zero. In the centre of the GCs which we choose to be inside the distance of the 300th star of each simulation to avoid low number statistics in the bins, we extrapolate the density profiles by setting it to the constant value of the innermost shell.

### 3.3.4 Potential

From the density profile we can compute the potential using the Poisson Equation (4) as described in Section 2.3. The potential is very important to calculate the energy and the radial action as well as for the orbit integration (see Section 2.4). We treat the potential of the GCs as being the superposition of the potential generated by the stellar mass density and a Kepler potential of a point mass (see Equation (8) in Section 2.3.3) for the IMBH.

In Figure 13 we plot the potential against the radius in units of the half-mass radii. SIM 1 and SIM 2 have almost the same potential. They are the same simulation at different ages. The simulation lost 5 % of its stars with 10 % of the total mass while the IMBH gained 13 %. The potential of the stars becomes more shallow while the potential of the IMBH became deeper. In the centre of the GCs, the negative potential rises quickly. SIM 3 and SIM 4 show a cored potential which is almost constant. SIM 4 shows a decreasing potential at 0.5 half-mass radii. In the outer regions all potentials tend to zero.

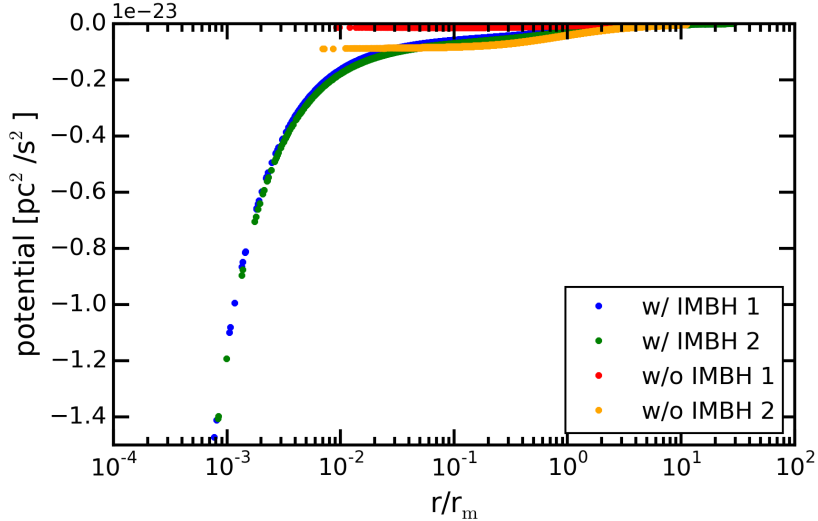


Figure 13: Potential of all GCs versus the radii in units of half-mass radii. SIM 1 and SIM 2 are almost identical. The GCs without IMBH remain constant in the inner part (until 0.5 half-mass radii) and decrease from the points where their densities decrease.

### 3.4 Investigations in action and integral of motion space

Now we change our investigations from phase space to orbit space. We do this by calculating the classical integrals of motions given by Equations (15) and (13) (see Section 2.4.1) and the actions, especially the radial action given by Equations (??) in Section 2.4.3. We have a look at the energies and angular momenta of the stars and compare them with the radial actions. We do not investigate  $J_\theta$  and  $J_\phi$  because the stellar systems are isotropic and spherical. A separation of the total angular momentum in a z-component  $J_\phi = L_z$  (with respect to a randomly chosen z-plane) and a component  $J_\theta = L - |L_z|$  does not seem useful since each orbit lies in a plane and these planes are evenly distributed. Therefore we consider just the total angular momentum. Our main goal is to find any systematic signatures for the simulations with IMBHs that can be considered as the direct evidence of the dynamical effect of the IMBH itself. For this reason we investigate selected stars which show an abnormal behaviour in the above-mentioned plots and compare them to the rest of the data to see where we find them. In the following histograms, the color indicates the number of stars.

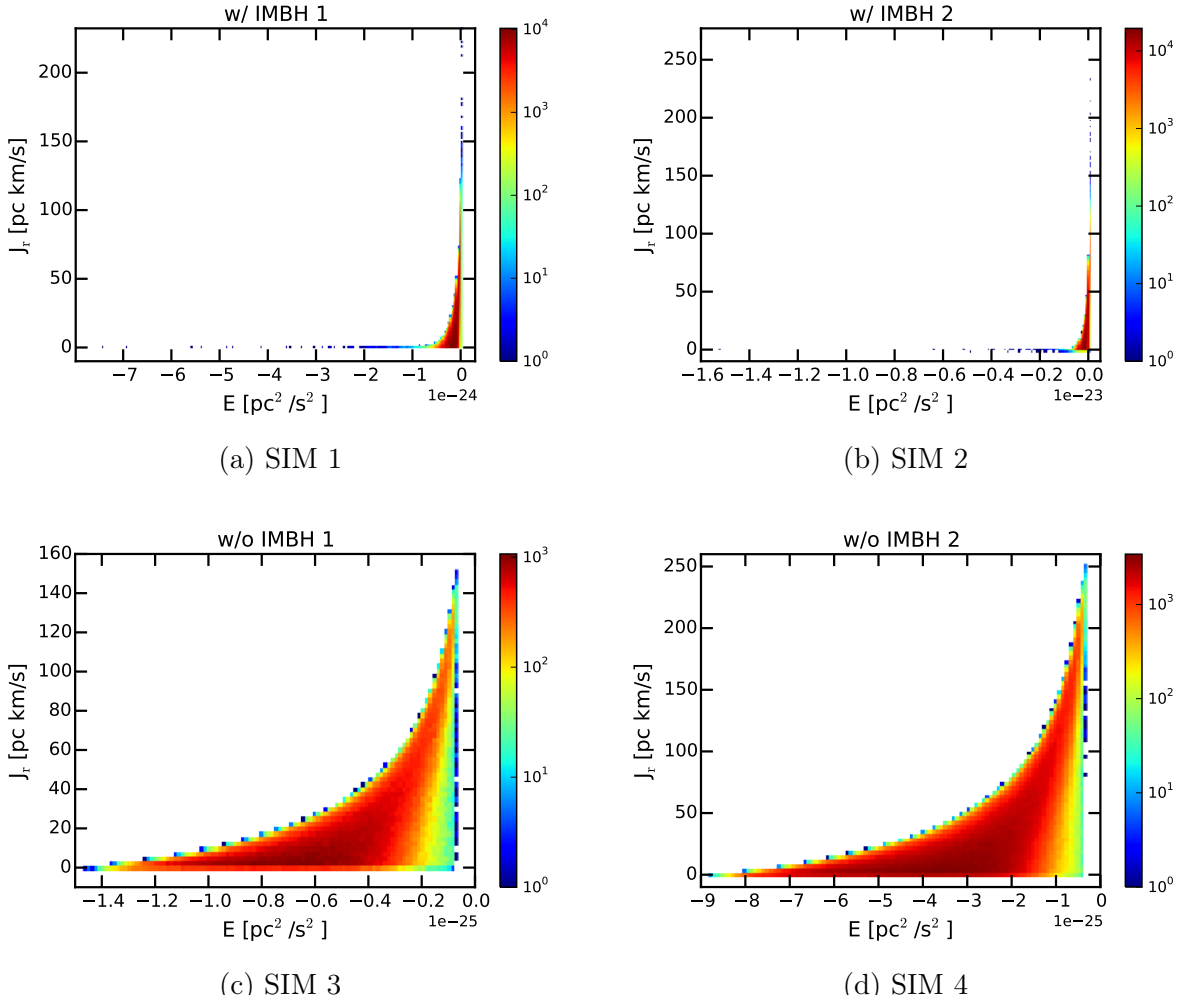


Figure 14: Radial action over energy. In Panels (a) and (b) it is plotted for both simulations with IMBH and the lower panels are for the simulation without IMBH. We find the crescent shape from Panels (c) and (d) clearly in Panels (a) and (b). But in SIM 1 and SIM 2 there are some stars differing from this shape. Some have high energy with no radial actions (henceforth referred to as "group 1") while others have high radial actions with almost no energy (henceforth "group 2").

### 3.4.1 Radial action versus energy

In Figure 14, we plot the radial action  $J_r$  versus the energy of the star as histograms for all GCs. We see many stars having a radial action significantly different than zero. That means we have many stars moving on eccentric orbits as expected from the radial anisotropy measured in Figure 10a in Section 3.3.2. We can recognize the shape given in Panels 14c and 14d also in the Panels 14a and 14b but in these panels we clearly see some outlier stars with significantly different integrals of motion. These outlier stars either have a radial action close to zero and a high negative total energy (below  $-9 \times 10^{-25} \text{ pc}^2/\text{s}^2$ , henceforth called "group 1") or almost an energy close to zero and high radial action (above  $150 \text{ pc km/s}$ , henceforth called "group 2").

We check the effective potential of the stars of the group to get information of their orbits and their actual positions. In Figure 15, we show one exemplary graph for each group taken from SIM 1.

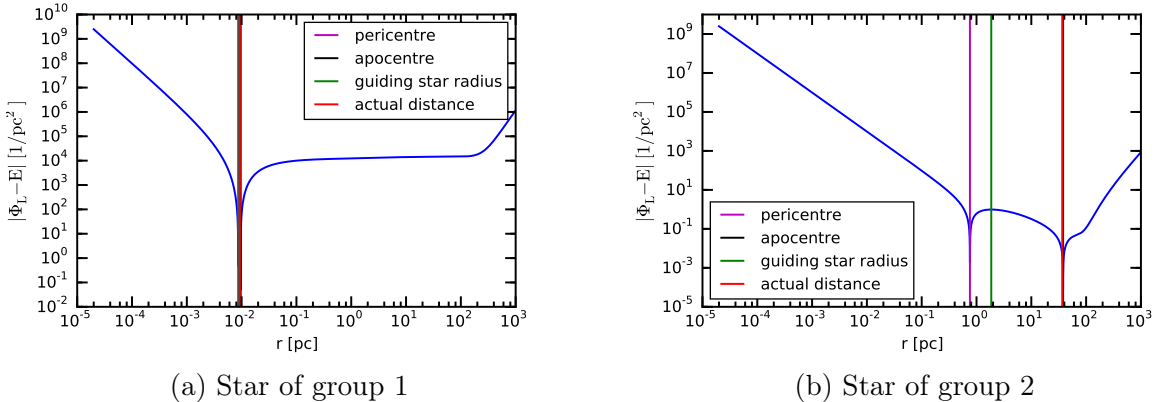


Figure 15: Effective potential of exemplary stars of both groups from Figure 14. The star of group 1 is clearly on a circular orbit with  $r_{\min} \approx r_g \approx r \approx r_{\max}$ . The star of group two has a highly eccentric orbit and its actual position is in its apocentre.

The first group of stars of SIM 1 contains 280 of the nearest 768 stars, including 85 % of the first 100 stars. Since they have radial actions close to zero they are on circular orbits. They have high negative total energy due to the very deep potential well of the IMBH (see Figure 13). We can clearly see this circular orbit in the root of the effective potential in Figure 15a. There, the peri- and the apocentre are the same which is typical for a circular orbit.

The nearest 30 stars on circular orbits around the IMBH are certainly bound to the IMBH. That is why we do not see this signature for SIM 3 and SIM 4. The other stars

of this group are likely to be bound to the IMBH as well, while the rest of the near stars which are not in this group seem to be near to or in their pericentre on more eccentric orbits and therefore potentially not bound to the IMBH.

The second group of stars with high radial actions and almost no energy includes 20 stars and cannot be clearly related to the IMBH. 12 of them are some of the furthermost stars of the snapshot. All these stars are in their apocentre on very eccentric orbits (see Figure 15b). This high eccentricity could be caused by an interaction with the IMBH, but since most of their pericentres are at a few pc we cannot assume much interaction with the IMBH for those stars. Another reason that these stars do not occur in SIM 3 and SIM 4 can be due to different truncation prescriptions used in the simulations (see Figure 11). These stars are almost outside of the GCs and have a energy close to zero. That means their kinetic energies are almost as large as the gravitational potential. With just a little more kinetic energy they could escape the cluster. That is why they could already have been excluded in SIM 3 and SIM 4, as escapers.

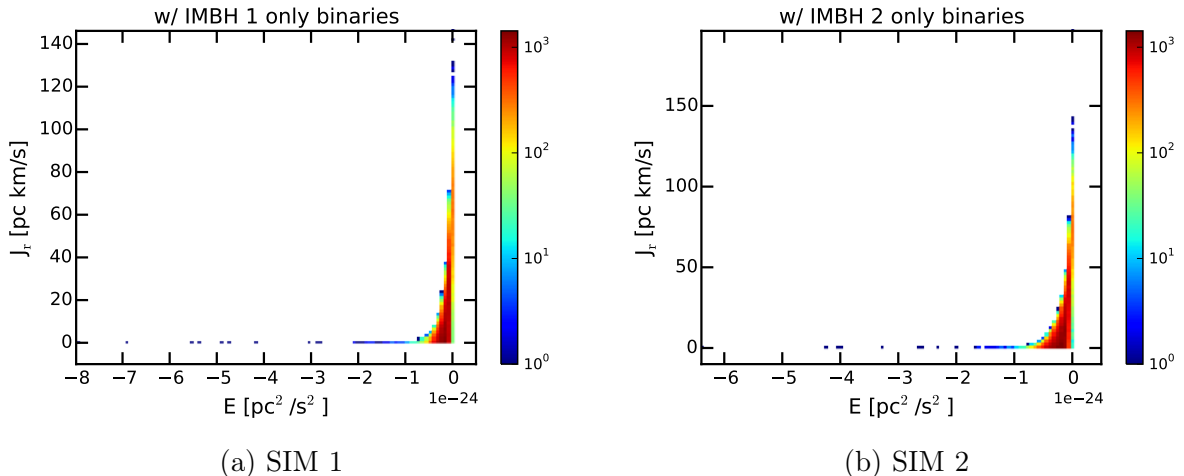


Figure 16: Radial action over energy only of binary systems of the GCs with IMBH. We see a similar distribution of stars as in Figure 14. Some binaries are on circular orbits while there are others with high radial action.

We might get these outlier stars from former binaries which were divided earlier in the evolution of the GC. One of the stars could have been captured on a circular orbit near the centre while the other could have been skid to a very eccentric orbit or to an unbound orbit and have left the system. To check this we will plot the same values only for our actual binary systems. As we see in Figure 16 the binary systems are behaving like single stars. There are binaries on circular orbits as well as some with high radial action. That could be an explanation for these outlier stars but it is not necessarily the

explanation for these stars.

### 3.4.2 Radial action versus angular momentum

Next we plot the radial actions over the absolute angular momenta of the stars of the simulations again as histograms. In Figure 17, we can see a triangular shape which seems characteristic for all simulations. Inside this shape we see in Figures 17a and 17b some substructure in the GCs with IMBH. As said in Section 2 we use only the specific quantities per unit stellar mass. Since this could be a reason for this substructure, we show the same histogram multiplying the masses of the stars to the (specific) angular momenta and the (specific) radial actions. In the Panels 17e and 17f we show this for SIM 1 and SIM 4. They show the same shape so this signature is clearly given by using specific values. This mass-dependent correlation could be due to dynamical mass segregation. Apart from that we do not see a signature of the IMBH in this plot.

### 3.4.3 Investigation of stars bound to the intermediate mass black hole

Now we want to investigate the stars of group 1 more in detail. We plot again the radial actions over energy and angular momentum but only for stars having a energy below  $-9 \times 10^{-25} \text{ pc}^2/\text{s}^2$ . In Figure 18 we see in Panels (a) and (b) the radial actions over the energies and in Panels (c) and (d) the radial actions over angular momenta. In the energy plots we see that the highest radial actions (up to  $1.5 \text{ pc km/s}$ ) are at the lowest total negative energies. The higher the total negative energy the lower the radial action. Only the stars with a radial action of zero are on circular orbits. Due to possible statistical noise we cannot interpret Panels (a) and (b) quantitatively. But we see that not all stars which seem to be at zero in Figures 14a and 14b are exactly at zero. In the angular momentum plots we see a linear correlation between radial action and angular momentum. The higher the angular momentum the lower the radial action.

### 3.4.4 Radial action versus guiding-star radius

We want to examine the spatial distribution of the radial actions to see outlier stars reveal a spatial signature. Therefore we check the values of the radial actions depending on the guiding-star radii. In Figure 19, the radial actions are plotted over their guiding-star distances. We highlight the stars of group 1 and group 2 taken from Figure 14 for SIM 1 and SIM 2. In general, there are several stars which have a really small guiding-star radius (up to  $10^{-5} \text{ pc}$ ). In SIM 3 and SIM 4 only very few stars go below 0.1 pc.

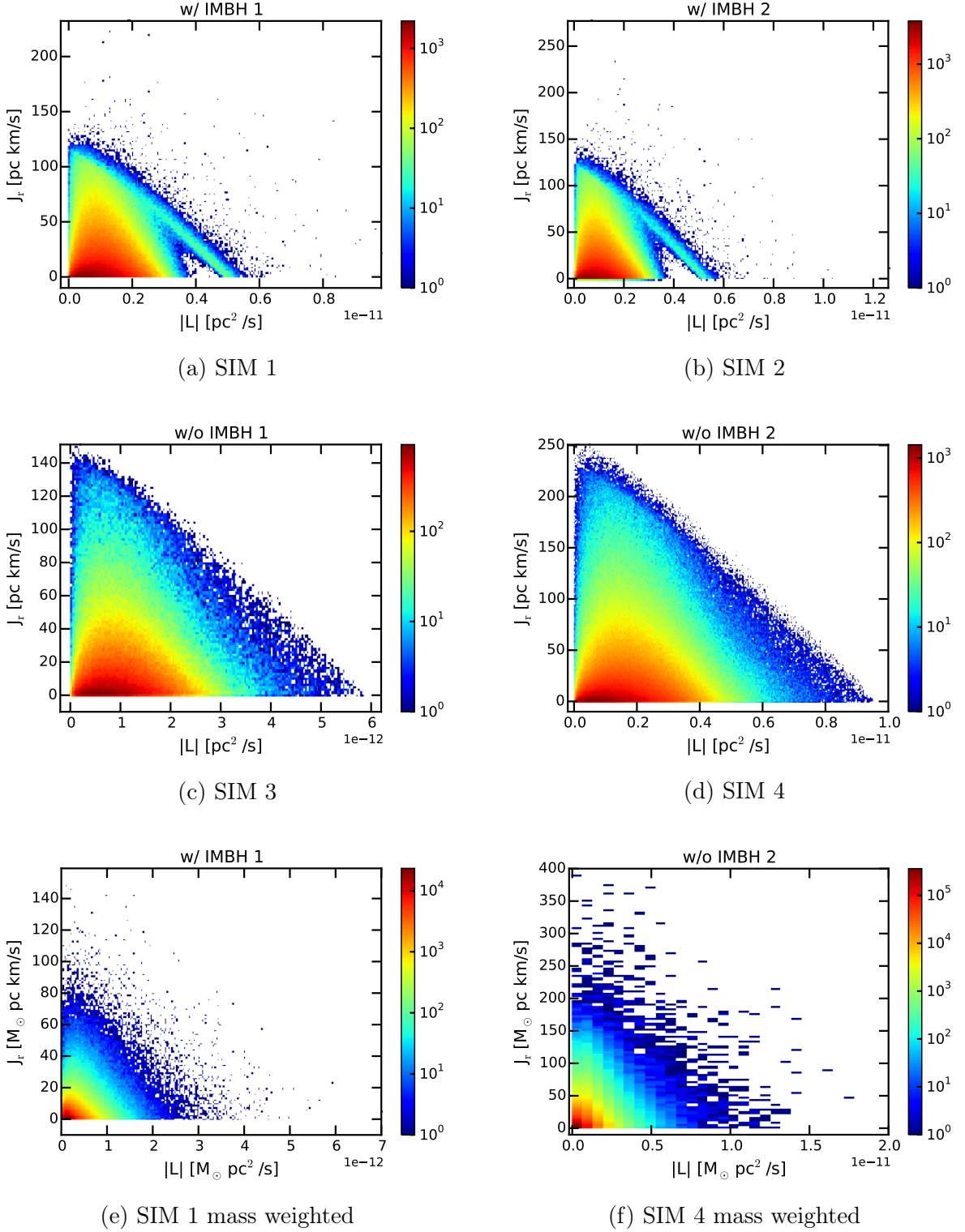


Figure 17: Radial action over angular momentum. Panels (c) and (d) look again very similar to each other with no recognizable substructure. In the Panels (a) and (b) we can clearly see a substructure from about 0.3 to about 0.6  $\text{pc}^2/\text{s}$  in almost the whole radial action range. In Panels (e) and (f) we multiply the (specific) angular momenta and (specific)radial actions with the masses of the stars for SIM 1 and SIM 4. They look similar to each other.

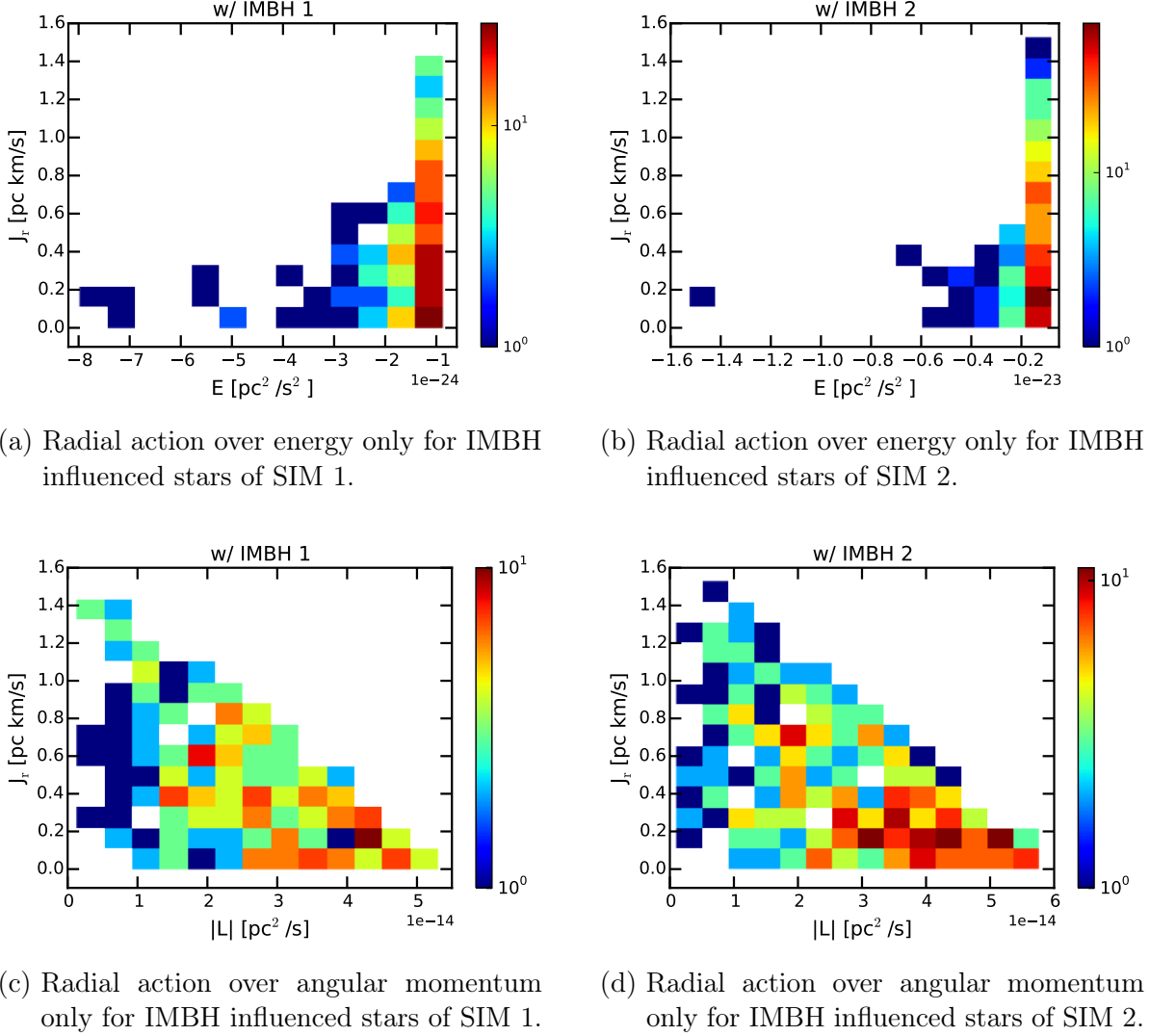


Figure 18: Close-up of radial action versus energy and angular momentum for group 1 stars. In the Panels (a) and (b) the radial action is shown versus the energy while in Panels (c) and (d) it is shown versus the angular momentum. The more circular the orbit, the lower the total energy and therefore deeper the star is caught in the deep potential well of the IMBH. A linear correlation is clearly visible in the angular momentum plots. The higher the angular momentum the lower the radial action.

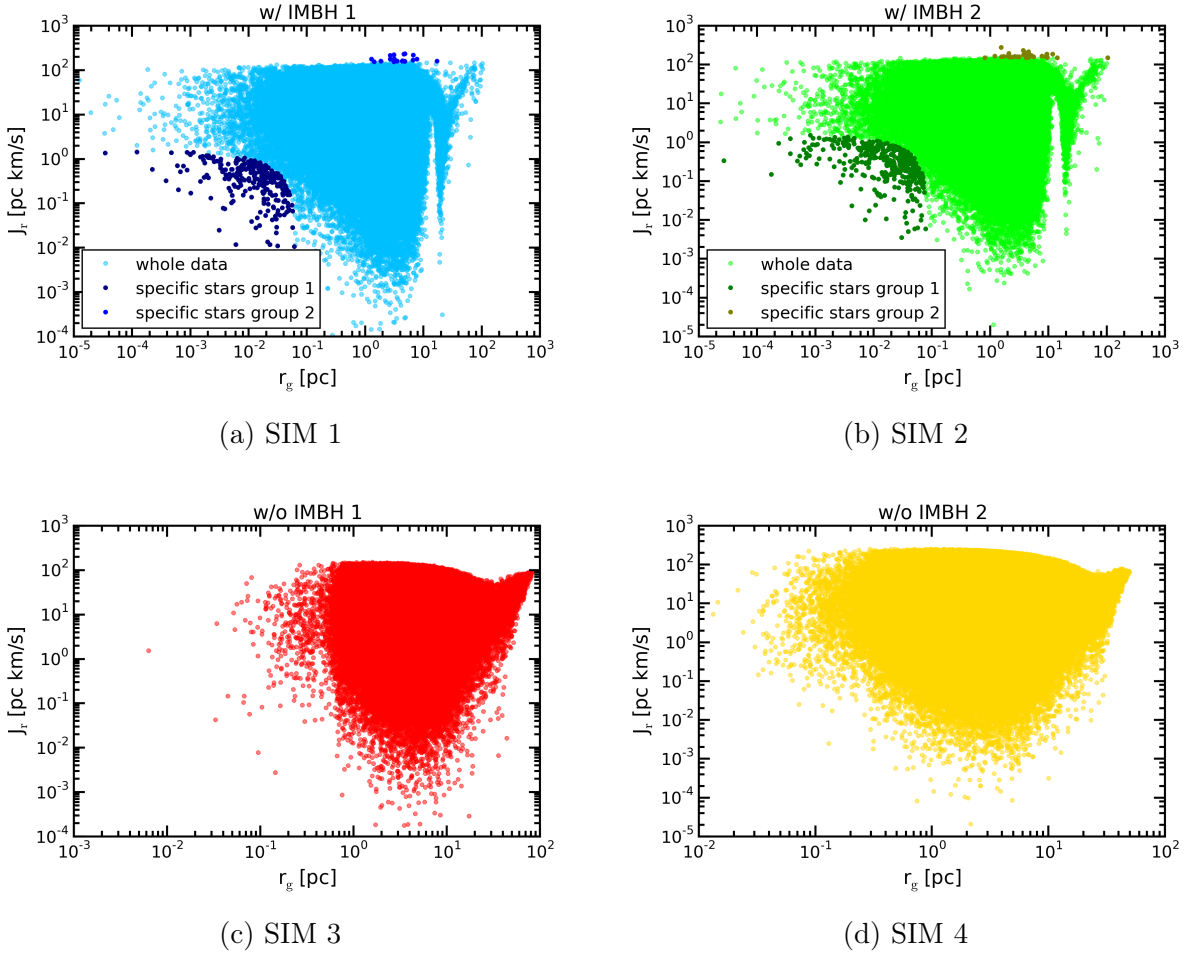


Figure 19: Radial action over guiding-star radius with marked specific stars on a double logarithmic scale. The colors are given as in Figure 10. All simulations have a similar shaped distributions except for the marked stars which are the ones belonging to group 1 and 2 (see Figure 14). The GCs without IMBH have almost no stars below 0.1 pc, while the other simulations go down until  $10^{-5}$  pc including the stars of group 1. There is a gap in SIM 1 and SIM 2 from about 10 to 20 pc. Due to this high distances this gap is most likely not a signature of the IMBH but probably due to numerical inaccuracies.

We see a round border of the shape given by stars of group 1. It is really clear to see but only if we know which stars we have to select. We cannot draw this conclusion the other way around, i.e. selecting these star in this plot and select them in Figure 14. The sharp signatures in Figures 19a and 19b at large guiding-star radii are probably due to numerical issues with deriving the guiding-star radius. But they do not affect the conclusion about signatures of the IMBH, as these stars are in general far away from the IMBH.

## 4 Results & Discussion

In this chapter we summarize and give an overview of the results of Chapter 3 (Section 4.1), discuss problems and assumptions throughout the work, strengthen the outcome of this thesis by showing our key plot again for actions calculated in a wrong calculated potential in Section 4.2 and give a future perspective in Section 4.3.

### 4.1 Signatures of intermediate mass black holes in action space

In Section 3.4 we got some clear differences between the simulations with and without IMBH, and we took them as signatures of the IMBH. For SIM 1, we juxtapose the three signature plots containing the radial actions and mark the stars of the different groups. Group 1 (yellow) includes the stars with high negative energies and low radial actions which are most likely bound or affected by the IMBH. Group 2 (red) contains the stars having an total energy close to zero and high radial actions. These could be different to SIM 3 and SIM 4 only due to different truncation prescriptions since the stars are located in the outer region of the GC. Group 3 (blue) contains all stars having a guiding-star radius below 0.1 pc, that are only there for the simulations with IMBH.

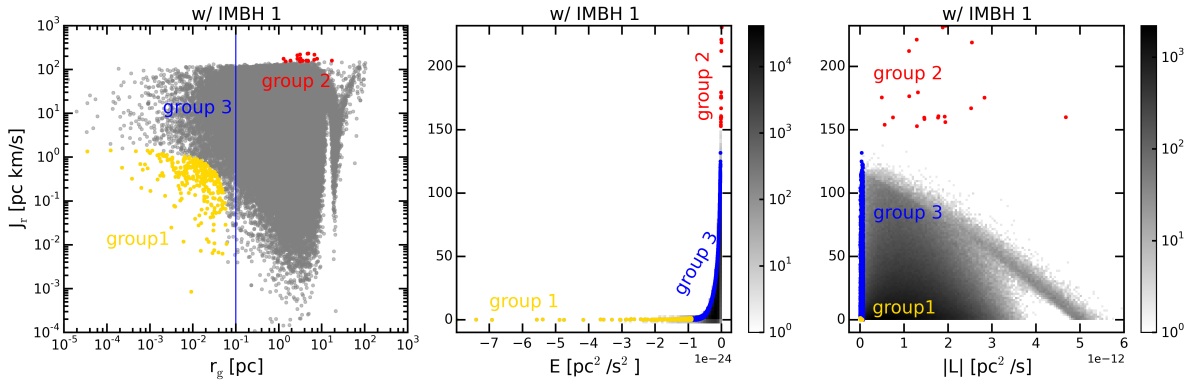


Figure 20: Radial action over different values with marked groups of stars. In the first panel the radial action is plotted versus the guiding star radius, in the next panel as histogram over the energy and in the last panel as histogram over the angular momentum. Group 1 marked yellow includes all stars having an energy below  $9 \times 10^{-25} \text{ pc}^2/\text{s}^2$ . Group 2 (red) marks all stars having a radial action over  $150 \text{ pc km/s}$ . Group 3 in blue contains all stars having a guiding star radius below 0.1 pc.

Figure 20 is divided into three panels. In all panels the whole simulation is given in grey, in the second and third panel it is color coded with the number of the stars per bin.

The different groups are color coded as mentioned above. In the first panel we see the different groups, their guiding-star radii and their radial actions. Group 1 is included in group 3 and is the part with the lowest radial actions. It has a clear round shape which could be another significant property.

The second panel shows the histogram of the radial action over the energy. This is the plot where we can clearly see and select the stars of group 1 and group 2. Group 1 stars are on the bottom of the plot where the radial action is almost zero and the energy is very high. Group 2 stars are located at energies close to zero with high radial action. The stars of group 3 cannot be directly seen here. For each energy they have the highest occurring radial action and are located along the upper edge of the main shape which is best seen in Figures 14c and 14c. Since the stars of group 3 have only small guiding-star radii they should not have far-off apocentres but they can have pericentres close to the black hole. Having the highest radial actions at given energies these stars have very eccentric orbits.

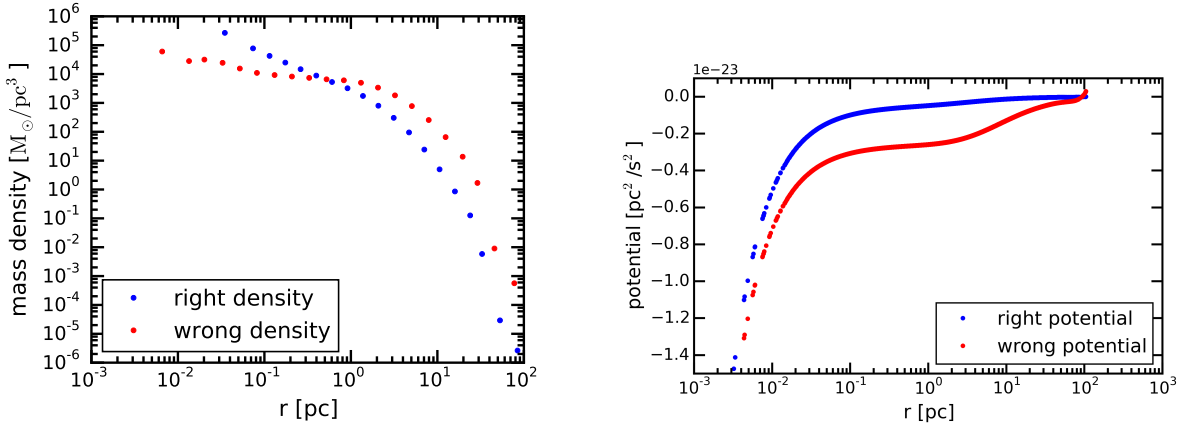
The third plot is the radial action versus angular momentum histogram. Group 1 and group 3 stars cannot be distinguished from other stars in there, since given small guiding-star radius they have only a small angular momentum. There are many other stars not belonging to group 1 nor group 3 which have a very small angular momentum as well. Only stars of group 2 can be seen above a radial action of  $150 \text{ pc km/s}$ . But this plot reveals something else: the mass dependency of the radial actions and the angular momentum. We clearly see a substructure from  $0.3$  until  $0.6 \text{ pc}^2/\text{s}$  independent of all groups. In Figure 17 we have seen that this substructure is due to the mass dependence.

To summarize, stars in group 1 are a clear signature of a presence of an IMBH and they can be detected as a tail at high energy in the radial action versus energy plot. These stars are indeed the closest to the IMBH (small guiding star radius), and have very circular orbits. Therefore we interpret them as bound stars to the IMBH. They are not observed in the simulations without IMBH.

## 4.2 Robustness of the results: using a wrong potential

One test to re-check our results is to use a randomly wrong stellar mass density which is the basis of all our calculations. In Figure 21, we compare the right and the wrong density.

With this wrong potential we can also get the key plot from Section 4.1 given in Figure 22. In this figure, we have the same color coding as in Figure 20. We see the three groups at the same positions. In the first panel, group 1 again reveals the round



- (a) Density profiles of right and wrong density of SIM1. While the right density has a gentle gradient the wrong density exhibits a core profile in the central part and a steep gradient in the outer part. In the central part, the density is too low while in the outer part it is higher than the right one.
- (b) Potential versus radius of right and wrong density of SIM1. The right potential has a steep gradient in the centre of the GC and flattens rapidly. The wrong potential is always higher in absolute values and has a two step flattening. The first flattening is at the same distance as the one from the right potential but from there it is much higher than the right potential. The second flattening step is where the density profile starts falling rapidly.

Figure 21: Comparison of right (blue) and wrong (red) calculated density and potential of SIM 1.

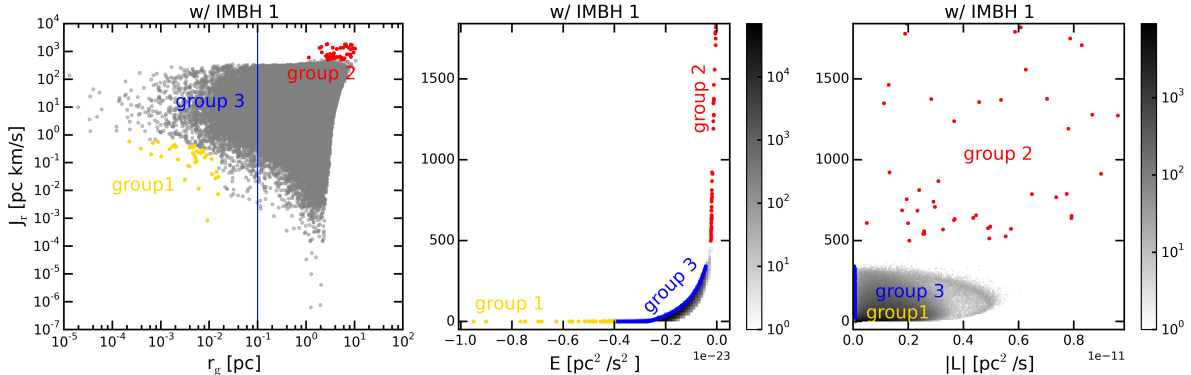


Figure 22: Radial action over guiding-star radius, energy and angular momentum, computed using a wrong potential. Stars in each group are marked as in Figure 20. Group 1 (yellow) includes all stars having an energy below  $4 \times 10^{-24} pc^2/s^2$ . Group 2 (red) marks all stars having a radial action over  $500 pc km/s$ . Group 3 in blue contains all stars having a guiding star radius below  $0.1 pc$ . All the conclusions reported in Section 4.1 still hold even when using a wrong potential.

shape. In the second panel, we can select again group 1 and group 2 stars. This time the fraction of group 2 stars is higher than the fraction of group 1 stars. In the third panel, there is a similar substructure to the third panel of Figure 20 independent of the stars of the groups.

This test shows us that this method is not very sensitive to the potential generated by stellar masses. This guarantees a robustness for observational approaches where the true potential is extremely hard to compute because of its uncertainty. The same test should be done changing the potential of the IMBH since we have no a priori information about its mass.

### 4.3 Discussion and future perspectives

In summary we can say that we found clearly evidence of the IMBH in the radial actions by plotting them versus the energy and the guiding-star radius. To get there we made some simplified assumptions which should be investigated in more detail in future work.

One of the assumptions concerns the density profile. In this depends our action approach because it is necessary to calculate the potential and from that the actions. Since there is not a simple analytical function that can describe the whole profile we interpolated the binned densities and set the central density equal to the innermost density bin. Another approach to describe stellar density and potential more accurately could be a Multi-Gaussian Expansion fit (see, for example, Emsellem *et al.*, 1994; Cappellari, 2002) to the stellar density profile. But as shown in Section 4.2 smaller errors in the stellar density, e.g. due to interpolation and extrapolation, should not affect the results too much. We tested the stability of our procedure by changing different values for the stellar mass densities, as explained in the previous section. As a result we see that the results for Section 4.1 do not change. Another test in further investigation would be changing the potential of the IMBH since in observation we cannot yet constrain it. This would show the sensitivity of our results to the particular choice of IMBH potential made.

Another problem that might have affected our results is the differences of the simulations for GCs with and without IMBH. Since they have different initial conditions and conditions throughout the simulating process we cannot compare them directly. In particular the radial actions cannot be compared quantitatively. We see the differences directly in the distributions (Figures 5 and 6) and in the anisotropy in the outer parts, possibly due to different truncation prescriptions. In further investigations we should consider using simulations with same conditions with only the absence of an IMBH in

one of the simulations.

Some physical assumptions have been that actions stay totally constant over time or rather that we have only looked at them at the time of the snapshot. Changing integrals of motion goes along with changing orbits which could have some numerical fluctuations especially near the IMBH.

Another assumption is that we mostly use specific values. We see in Figure 17 that there can be distortion due to that. Further work should investigate the mass dependency of the integrals of motion since this is very important. The stars in GCs have different masses and display mass-dependent kinematics due to mass segregation / partial energy equipartition.

Finally, if all these points are applied to this method we should then think of a way to apply this approach to observational-like data. The main problem is that we do not have the 3D spatial information (we only have the projected x and y while z is missing) and only for few stars the 3D kinematics are known.

## 5 Conclusion

In this work we investigated simulated GCs in orbit space, specifically in action space, to figure out if we can use this method to find signatures of IMBHs. Given four simulations two of which containing an IMBH we first examined the properties in color-magnitude and in phase space. Generating the potentials of the simulations from their density profiles we calculated integrals of motion for all the GC stars. Due to the spherically symmetric potential of the GCs only the energy and the total angular momentum as classical integrals of motion and particularly the radial action as best choice of integral of motions were relevant to us. We found a clear signature of IMBHs in the distribution of stars in the specific radial action versus specific energy plane. More but less clear signatures were found in a distribution of the radial action versus the guiding star radius and in a distribution of the radial action versus the angular momentum. The robustness of these signatures was tested, using a wrong density as a base of our calculations. Further investigations have to be done, i.e. by changing the Kepler potential of the IMBH and comparing the simulations with exact identical initial conditions and as only difference the presence of an IMBH. Then we will have to think about how to adapt our method for an application to observational data.

## 6 Acronyms

- CMD** color magnitude diagram
- COM** centre of mass
- DF** distribution function
- GC** globular cluster
- HST** Hubble Space Telescope
- IMBH** intermediate mass black hole
- MW** Milky Way
- SMBH** super massive black hole
- SSP** single stellar population

## References

- Bahcall, J.N. and Wolf, R.A. “Star distribution around a massive black hole in a globular cluster”. *ApJ*, **209**, 214–232, 1976.
- Bartelmann, M. “Theoretische Physik I: Punktmechanik und mathematische Methoden”. 2007.
- Bellini, A., Anderson, J., van der Marel, R.P., Watkins, L.L., King, I.R., Bianchini, P., Chanamé, J., Chandar, R., Cool, A.M., Ferraro, F.R., Ford, H., and Massari, D. “Hubble Space Telescope Proper Motion (HSTPROMO) Catalogs of Galactic Globular Clusters. I. Sample Selection, Data Reduction, and NGC 7078 Results”. *ApJ*, **797**, 115, 2014.
- Bianchini, P., Norris, M.A., van de Ven, G., and Schinnerer, E. “Understanding the central kinematics of globular clusters with simulated integrated-light IFU observations”. *MNRAS*, **453**, 365–376, 2015.
- Bianchini, P., Varri, A.L., Bertin, G., and Zocchi, A. “Rotating Globular Clusters”. *ApJ*, **772**, 67, 2013.
- Binney, J. “Henon’s Isochrone Model”. *ArXiv e-prints*, 2014.
- Binney, J. and Tremaine, S. *Galactic Dynamics: Second Edition*. Princeton University Press, 2008.
- Bovy, J. “galpy: A python Library for Galactic Dynamics”. *ApJS*, **216**, 29, 2015.
- Bovy, J. and Rix, H.W. “A Direct Dynamical Measurement of the Milky Way’s Disk Surface Density Profile, Disk Scale Length, and Dark Matter Profile at 4 kpc  $\sim$  R  $\sim$  9 kpc”. *ApJ*, **779**, 115, 2013.
- Bressan, A., Marigo, P., Girardi, L., Salasnich, B., Dal Cero, C., Rubele, S., and Nanni, A. “PARSEC: stellar tracks and isochrones with the PAdova and TRieste Stellar Evolution Code”. *MNRAS*, **427**, 127–145, 2012.
- Cappellari, M. “Efficient multi-Gaussian expansion of galaxies”. *MNRAS*, **333**, 400–410, 2002.
- Carroll, B.W. and Ostlie, D.A. *An introduction to modern astrophysics and cosmology*. 2006.

- Downing, J.M.B., Benacquista, M.J., Giersz, M., and Spurzem, R. “Compact binaries in star clusters - I. Black hole binaries inside globular clusters”. *MNRAS*, **407**, 1946–1962, 2010.
- Emsellem, E., Monnet, G., and Bacon, R. “The multi-gaussian expansion method: a tool for building realistic photometric and kinematical models of stellar systems I. The formalism”. *A&A*, **285**, 1994.
- Ferrarese, L. and Merritt, D. “A Fundamental Relation between Supermassive Black Holes and Their Host Galaxies”. *ApJ*, **539**, L9–L12, 2000.
- Giersz, M. “Monte Carlo simulations of star clusters - I. First Results”. *MNRAS*, **298**, 1239–1248, 1998.
- Giersz, M., Leigh, N., Hypki, A., Lützgendorf, N., and Askar, A. “MOCCA code for star cluster simulations - IV. A new scenario for intermediate mass black hole formation in globular clusters”. *MNRAS*, **454**, 3150–3165, 2015.
- Gillessen, S., Eisenhauer, F., Trippe, S., Alexander, T., Genzel, R., Martins, F., and Ott, T. “Monitoring Stellar Orbits Around the Massive Black Hole in the Galactic Center”. *ApJ*, **692**, 1075–1109, 2009.
- Harris, W.E. “A Catalog of Parameters for Globular Clusters in the Milky Way”. *AJ*, **112**, 1487, 1996.
- Hypki, A. and Giersz, M. “MOCCA code for star cluster simulations - I. Blue stragglers, first results”. *MNRAS*, **429**, 1221–1243, 2013.
- Kacharov, N., Bianchini, P., Koch, A., Frank, M.J., Martin, N.F., van de Ven, G., Puzia, T.H., McDonald, I., Johnson, C.I., and Zijlstra, A.A. “A study of rotating globular clusters. The case of the old, metal-poor globular cluster NGC 4372”. *A&A*, **567**, A69, 2014.
- Kirsten, F. and Vlemmings, W.H.T. “No evidence for a central IMBH in M 15”. *A&A*, **542**, A44, 2012.
- Kroupa, P. “On the variation of the initial mass function”. *MNRAS*, **322**, 231–246, 2001.

- Lanzoni, B., Mucciarelli, A., Origlia, L., Bellazzini, M., Ferraro, F.R., Valenti, E., Miocchi, P., Dalessandro, E., Pallanca, C., and Massari, D. “The Velocity Dispersion Profile of NGC 6388 from Resolved-star Spectroscopy: No Evidence of a Central Cusp and New Constraints on the Black Hole Mass”. *ApJ*, **769**, 107, 2013.
- Lützgendorf, N., Gebhardt, K., Baumgardt, H., Noyola, E., Neumayer, N., Kissler-Patig, M., and de Zeeuw, T. “Re-evaluation of the central velocity-dispersion profile in NGC 6388”. *A&A*, **581**, A1, 2015.
- Lützgendorf, N., Kissler-Patig, M., Gebhardt, K., Baumgardt, H., Noyola, E., de Zeeuw, P.T., Neumayer, N., Jalali, B., and Feldmeier, A. “Limits on intermediate-mass black holes in six Galactic globular clusters with integral-field spectroscopy”. *A&A*, **552**, A49, 2013.
- Lützgendorf, N., Kissler-Patig, M., Noyola, E., Jalali, B., de Zeeuw, P.T., Gebhardt, K., and Baumgardt, H. “Kinematic signature of an intermediate-mass black hole in the globular cluster NGC 6388”. *A&A*, **533**, A36, 2011.
- Maccarone, T.J. and Servillat, M. “Radio observations of NGC 2808 and other globular clusters: constraints on intermediate-mass black holes”. *MNRAS*, **389**, 379–384, 2008.
- Marigo, P., Girardi, L., Bressan, A., Groenewegen, M.A.T., Silva, L., and Granato, G.L. “Evolution of asymptotic giant branch stars. II. Optical to far-infrared isochrones with improved TP-AGB models”. *A&A*, **482**, 883–905, 2008.
- Meylan, G. and Heggie, D.C. “Internal dynamics of globular clusters”. *A&A Rev.*, **8**, 1–143, 1997.
- Miller, M.C. and Hamilton, D.P. “Production of intermediate-mass black holes in globular clusters”. *MNRAS*, **330**, 232–240, 2002.
- Mohr, P.J., Newell, D.B., and Taylor, B.N. “CODATA Recommended Values of the Fundamental Physical Constants: 2014”. *ArXiv e-prints*, 2015.
- Noyola, E., Gebhardt, K., and Bergmann, M. “Gemini and Hubble Space Telescope Evidence for an Intermediate-Mass Black Hole in  $\omega$  Centauri”. *ApJ*, **676**, 1008-1015, 2008.
- Piffl, T., Binney, J., McMillan, P.J., Steinmetz, M., Helmi, A., Wyse, R.F.G., Bienaymé, O., Bland-Hawthorn, J., Freeman, K., Gibson, B., Gilmore, G., Grebel, E.K., Koropatsis, G., Navarro, J.F., Parker, Q., Reid, W.A., Seabroke, G., Siebert, A., Watson,

F., and Zwitter, T. “Constraining the Galaxy’s dark halo with RAVE stars”. MNRAS, **445**, 3133–3151, 2014.

Piotto, G., Milone, A.P., Bedin, L.R., Anderson, J., King, I.R., Marino, A.F., Nardiello, D., Aparicio, A., Barbuy, B., Bellini, A., Brown, T.M., Cassisi, S., Cool, A.M., Cunial, A., Dalessandro, E., D’Antona, F., Ferraro, F.R., Hidalgo, S., Lanzoni, B., Monelli, M., Ortolani, S., Renzini, A., Salaris, M., Sarajedini, A., van der Marel, R.P., Vesperini, E., and Zoccali, M. “The Hubble Space Telescope UV Legacy Survey of Galactic Globular Clusters. I. Overview of the Project and Detection of Multiple Stellar Populations”. AJ, **149**, 91, 2015.

Plummer, H.C. “On the problem of distribution in globular star clusters”. MNRAS, **71**, 460–470, 1911.

Rubin, V.C., Ford, W.K.J., and Thonnard, N. “Rotational properties of 21 SC galaxies with a large range of luminosities and radii, from NGC 4605 /R = 4kpc/ to UGC 2885 /R = 122 kpc/”. ApJ, **238**, 471–487, 1980.

Sanders, J.L. and Binney, J. “Extended distribution functions for our Galaxy”. MNRAS, **449**, 3479–3502, 2015.

Strader, J., Chomiuk, L., Maccarone, T.J., Miller-Jones, J.C.A., Seth, A.C., Heinke, C.O., and Sivakoff, G.R. “No Evidence for Intermediate-mass Black Holes in Globular Clusters: Strong Constraints from the JVLA”. ApJ, **750**, L27, 2012.

Trenti, M. and van der Marel, R. “No energy equipartition in globular clusters”. MNRAS, **435**, 3272–3282, 2013.

van der Marel, R.P. and Anderson, J. “New Limits on an Intermediate-Mass Black Hole in Omega Centauri. II. Dynamical Models”. ApJ, **710**, 1063–1088, 2010.

Williams, L.L.R., Barnes, E.I., and Hjorth, J. “Collisionless dynamics in globular clusters”. MNRAS, **423**, 3589–3600, 2012.

Zocchi, A., Bertin, G., and Varri, A.L. “A dynamical study of Galactic globular clusters under different relaxation conditions”. A&A, **539**, A65, 2012.

## Acknowledgements

First of all I would like to thank Dr. Glenn van de Ven for welcoming me in his friendly working group and giving me the opportunity to get to know the exciting field of dynamics. I am also thankful for his support by giving useful comments and advices relating my thesis.

My gratitude also goes to Prof. Rainer Spurzem for evaluating my thesis.

Special thanks to Wilma Trick and Paolo Bianchini for guiding me through my investigations, answering all my questions, helping me coding, giving further suggestion, discussing about results and proof reading my thesis.

Furthermore I would like to thank my parents Ivo and Sigrun for giving me the possibility and support to study.

Another big thanks to my boyfriend Alex for supporting me, listening to my problems and helping me with his advice whenever I needed it.

Last but not least I would like to thank my office mates, especially Alina and Melanie for helping and pushing each other, and all my other friends.

## **Erklärung**

Ich versichere, dass ich diese Arbeit selbstständig verfasst und keine anderen als die angegebenen Quellen und Hilfsmittel benutzt habe.

Heidelberg, den 03.03.2016,

---

Sophia Milanov